A HyperFlash and ÉCLAT view of the local environment and energetics of the repeating FRB 20240619D

Monthly Notices of the ROYAL ASTRONOMICAL SOCIETY

MNRAS **546,** 1–22 (2026) https://doi.org/10.1093/mnras/stag090
Advance Access publication 2026 January 20

A HyperFlash and ÉCLAT view of the local environment and energetics of the repeating FRB 20240619D

O. S. Ould-Boukattine [1,2★] A. J. Cooper [3] J. W. T. Hessels [1,2,4,5] D. M. Hewitt [2] S. K. Ocker [6,7] A. Moroianu [2] K. Nimmo [8] M. P. Snelders [1,2] I. Cognard [9,10] T. J. Dijkema [1,11] M. Fine [2,4,5] M. P. Gawroński,[12] W. Herrmann [13] J. Huang,[4,5] F. Kirsten,[1,14] Z. Pleunis [1,2] W. Puchalska [12] S. Ranguin [2] and T. Telkamp [11]

[1]*ASTRON, Netherlands Institute for Radio Astronomy, Oude Hoogeveensedijk 4, NL-7991 PD Dwingeloo, the Netherlands*
[2]*Anton Pannekoek Institute for Astronomy, University of Amsterdam, Science Park 904, NL-1098 XH Amsterdam, the Netherlands*
[3]*Astrophysics, The University of Oxford, Keble Road, Oxford OX1 3RH, UK*
[4]*Trottier Space Institute, McGill University, 3550 rue University, Montréal, QC H3A 2A7, Canada*
[5]*Department of Physics, McGill University, 3600 rue University, Montréal, QC H3A 2T8, Canada*
[6]*Cahill Center for Astronomy and Astrophysics, California Institute of Technology, MC 249-17 California Institute of Technology, Pasadena CA 91125, USA*
[7]*The Observatories of the Carnegie Institution for Science, Pasadena, CA 91101, USA*
[8]*MIT Kavli Institute for Astrophysics and Space Research, Massachusetts Institute of Technology, 77 Massachusetts Ave, Cambridge, MA 02139, USA*
[9]*Station de Radioastronomie de Nançay, Observatoire de Paris, PSL University, CNRS, Université d'Orléans, F-18330 Nançay, France*
[10]*Laboratoire de Physique et Chimie de l'Environnement et de l'Espace LPC2E UMR7328, Université d'Orléans, CNRS, F-45071 Orléans, France*
[11]*CAMRAS Dwingeloo Radio Telescope Foundation, Oude Hoogeveensedijk 4, NL-7991 PD Dwingeloo, the Netherlands*
[12]*Institute of Astronomy, Faculty of Physics, Astronomy and Informatics, Nicolaus Copernicus University, Grudziadzka 5, 87-100 Toruń, Poland*
[13]*Astropeiler Stockert e.V., Astropeiler 1-4, D-53902 Bad Münstereifel, Germany*
[14]*Department of Space, Earth and Environment, Chalmers University of Technology, Onsala Space Observatory, SE-439 92 Onsala, Sweden*

Accepted 2026 January 6. Received 2025 December 9; in original form 2025 September 19

ABSTRACT

Time-variable propagation effects provide a window into the local plasma environments of repeating fast radio burst (FRB) sources. Here we report high-cadence observations of FRB 20240619D, as part of the HyperFlash and ÉCLAT programmes. We observed for 500 h and detected 217 bursts, including 10 bursts with high fluence (>25 Jy ms) and implied energy. We track burst-to-burst variations in dispersion measure (DM) and rotation measure (RM), from which we constrain the parallel magnetic field strength in the source's local environment: 0.27 ± 0.13 mG. Apparent DM variations between sub-bursts in a single bright event are interpreted as coming from plasma lensing or variable emission height. We also identify two distinct scintillation screens along the line of sight, one associated with the Milky Way and the other likely located in the FRB's host galaxy or local environment. Together, these (time-variable) propagation effects reveal that FRB 20240619D is embedded in a dense, turbulent and highly magnetised plasma. The source's environment is more dynamic than that measured for many other (repeating) FRB sources, but less extreme compared to several repeaters that are associated with a compact, persistent radio source. FRB 20240619D's cumulative burst fluence distribution shows a power-law break, with a flat tail at high energies. Along with previous studies, this emphasises a common feature in the burst energy distribution of hyperactive repeaters. Using the break in the burst fluence distribution, we estimate a source redshift of $z = 0.042 - 0.240$. We discuss FRB 20240619D's nature in the context of similar studies of other repeating FRBs.

Key words: fast radio bursts – radio continuum: transients.

1 INTRODUCTION

Out of the thousands of fast radio burst (FRB) sources detected to date, about a half dozen are prolific repeaters that have been detected hundreds to thousands of times by various telescopes (e.g. CHIME/FRB Collaboration 2021; H. Xu et al. 2022; D. C. Konijn et al. 2024). When active, these 'hyperactive' repeaters may even contribute a significant fraction of the total observable all-sky rate of FRBs above a certain fluence limit ($22.0^{+15.6}_{-10.3}$ per cent R_{sky} ($\mathcal{F} > 500$ Jy ms), e.g. O. S. Ould-Boukattine et al. 2026). The majority of repeaters have repetition rates at least an order of magnitude lower (CHIME/FRB Collaboration et al. 2023, Fig. 9), and are roughly consistent with the upper limits on the rates of most apparent non-repeaters, making it difficult to establish two clearly separated types of FRBs (CHIME/FRB Collaboration

★ E-mail: ouldboukattine@astron.nl

2023; F. Kirsten et al. 2024). Though rare, hyperactive repeaters are valuable because they allow one to build a record of an FRB's activity as a function of radio frequency and time (e.g. D. M. Hewitt et al. 2022; J. N. Jahns et al. 2023). By measuring propagation effects like dispersion (J. W. T. Hessels et al. 2019), Faraday rotation (A. Gopinath et al. 2024), and scintillation/scattering (S. K. Ocker et al. 2023; K. Nimmo et al. 2025), we can also map dynamic effects along the line of sight and in the FRB's local environment. This information complements what we can glean from precision localisations within a host galaxy (D. M. Hewitt et al. 2024a; M. Bhardwaj et al. 2025; CHIME/FRB Collaboration et al. 2025). Together, these are the clues needed to differentiate between proposed FRB models, and to ascertain whether a single model can explain all sources.

Such studies are particularly valuable when full polarimetry, amplitude and phase data ('voltage'/'baseband' data) are available to flexibly study the bursts at a range of time and frequency resolutions. Exploring microsecond temporal structures can strongly constrain the dispersion measure (DM) and possible subtle variations (K. Nimmo et al. 2022), while wide-band polarimetry can detect rotation measure (RM) variations (e.g. Y. Li et al. 2025).

Some repeating FRBs have been found in extreme and dynamic magneto-ionic environments (D. Michilli et al. 2018; R. Anna-Thomas et al. 2023; A. M. Moroianu et al. 2026). The first-known repeater, FRB 20121102A, resides near an active star-forming region in low-metallicity dwarf host galaxy (C. G. Bassa et al. 2017; S. Chatterjee et al. 2017; S. P. Tendulkar et al. 2017). It shows both a highly variable DM and RM, and has been associated with a persistent radio source (PRS, B. Marcote et al. 2017) that is possibly a nebula powered by the FRB source. FRB 20190520B is another repeater whose bursts and host galaxy are remarkably similar to FRB 20121102A (R. Anna-Thomas et al. 2023). In contrast, the repeaters FRB 20180916B and FRB 20200120E have shown modest to no DM or RM variations and have no associated PRS down to stringent luminosity limits (K. Nimmo et al. 2021; R. Mckinven et al. 2023a). Repeating FRBs are found in a diverse range of galaxies and local environments–including globular clusters (F. Kirsten et al. 2022), dwarf galaxies (D. M. Hewitt et al. 2024b; A. M. Moroianu et al. 2026; M. Bhardwaj et al. 2025), star-forming spirals (B. Marcote et al. 2020), and ellipticals (T. Eftekhari et al. 2025; V. Shah et al. 2025) – raising the question of whether repeating FRBs share a common progenitor. Similarly, the connection between repeating FRBs and the dominant population of apparently non-repeating FRBs is currently unclear (see, e.g. F. Kirsten et al. 2024; CHIME/FRB Collaboration et al. 2025).

Previous studies have found that repeating FRBs are typically longer in duration and narrower in emission bandwidth compared to the apparently one-off bursts (Z. Pleunis et al. 2021). Repeaters also often show a time-frequency drift, where subbursts typically appear at lower frequencies at later times (colloquially termed the 'sad trombone' effect; J. W. T. Hessels et al. 2019; J. T. Faber et al. 2024). This suggests a different emission mechanism and potentially progenitor type. None the less, the hyperactive sources are clearly exceptionally active, and distinguish themselves from much of the known population. Burst energetics are another valuable point of comparison. High-cadence observations of repeaters have shown that high-energy bursts have a similar statistical distribution to the population of one-off bursts and can reach similarly high energies – implying that the source's total energy reservoir is comparable (F. Kirsten et al. 2024; O. S. Ould-Boukattine et al. 2026). This suggests a possible link, whereby the apparently one-off bursts may simply be the most energetic bursts from sources that will eventually repeat.

Table 1. Summary of known, measured, and inferred properties of FRB 20240619D.

Property	Values
Right Ascension (J2000, ICRS)[a]	$19^h49^m29.21^s$
Declination (J2000, ICRS)[a]	$-25°12'49.40''$
Uncertainty (RA & DEC)[a]	$0.9''$
Galactic longitude (ℓ)	$15.4559°$
Galactic latitude (b)	$-23.3294°$
Galactic scattering time-scale (1 GHz)[b]	0.73 μs
Galactic scattering time-scale (1.271 GHz)[b]	0.28 μs
Galactic scintillation bandwidth (1 GHz)[b]	251.3 kHz
Galactic scintillation bandwidth (1.271 GHz)[b]	655.7 kHz
DM_{disk} (NE2001)[b]	94.3 pc cm^{-3}
DM_{disk} (YMW16)[c]	62.7 pc cm^{-3}
Measured and inferred properties in this work	
Dispersion measure range	[464.857, 465.266] pc cm^{-3}
Rotation measure range	[−182.2, −279.8] rad m^{-2}
Scattering time-scale range (1 GHz)	[120, 2900] μs[d]
Galactic Scintillation bandwidth (1.271 GHz)	[74, 159] kHz
Extragalactic Scintillation bandwidth (1.271 GHz)	6.7 ± 0.7 kHz[e]
Parallel magnetic field strength ($B_\parallel$)	0.27 ± 0.13 mG
Redshift (z) upper limit Macquart (DM-z) relation	< 0.37
Redshift (z) estimate based on E_{break}	0.042-0.240

[a]From the MeerKat disovery paper (J. Tian et al. 2025).
[b]Calculated using the NE2001p model (J. M. Cordes & T. J. W. Lazio 2002; S. K. Ocker & J. M. Cordes 2024).
[c]Calculated using the YMW16 model (J. M. Yao, R. N. Manchester & N. Wang 2017).
[d]referenced to 1 GHz, see Section 3.4.
[e]Based on a single measurement, B01-Wb, see Section 3.5 and Fig. 7.

Recently, the MeerTRAP collaboration discovered a new hyperactive repeater, FRB 20240619D using the MeerKAT telescope (J. Tian et al. 2024, 2025). The source was revealed to be highly active due to the detection of 3 bursts within only 2 min. J. Tian et al. (2024) used their voltage data to localise FRB 20240619D to $\alpha = 19^h49^m29.21^s$, $\delta = -25°12'49.40''$ (J2000) with an uncertainty of 0.9 arcsec. Two optical sources were identified in the DESI Legacy Survey DR10 near the position of the FRB, but neither has a measured redshift (A. Dey et al. 2019) and the host galaxy of FRB 20240619D remains unknown. Table 1 provides an overview of the properties of FRB 20240619D. Follow-up observations by A. Kumar et al. (2024) and Y. Bhusare, Y. Maan & A. Kumar (2025) using the upgraded Giant Metrewave Radio Telescope (uGMRT) led to the detection of 60 bursts between 550–750 MHz in 2024 July and placed a 5σ upper limit on the association of a PRS of 417 μJy beam^{-1} at 650 MHz. FRB 20240619D provides a new opportunity to study a hyperactive repeater and to compare its energetics and local environment with the small sample of well-studied FRB sources.

In this paper, we report on a high-cadence observing campaign towards FRB 20240619D, totalling more than 500 h of observations spanning over 4 months and yielding 217 burst detections including 10 very-high-energy bursts (fluence > 25 Jy ms). These observations were carried out as part of the HyperFlash FRB monitoring campaign, with three 25-m radio telescopes located in Europe: The Westerbork RT-1 (Wb) and Dwingeloo (Dw) telescopes, both located in the Netherlands, and the Stockert telescope (St) located in Germany. Additionally, we also observed with the Nançay Radio Telescope (NRT) as part of the ÉCLAT observing programme. We measure the spectrotemporal burst properties for our sample to investigate time variability. Additionally, we compare the cumulative burst fluence distribution with other repeating FRB sources in the literature.

In Section 2, we describe the data acquisition, observational set-up, and burst search. Section 3 presents the analysis of the burst properties and time-variable propagation effects. In Section 4 we discuss our results and the summarise conclusions in Section 5.

2 OBSERVATIONS AND BURST SEARCH

We observed FRB 20240619D using several European radio telescopes, accumulating 504.1 h on source between 5 July 2024 (MJD 60496) to 2024 October 19 (MJD 60602). Our first observation started only 13 h after the announcement of the source's discovery ATel (J. Tian et al. 2024), as shown in the overview of our observational campaign in Appendix Fig. B1. Appendix Table 2 further summarises the observational campaign, including the fluence detection limits of each telescope.

2.1 HyperFlash and ÉCLAT

HyperFlash (PI: O. S. Ould-Boukattine) is a high-cadence monitoring program using 25-m diameter telescopes to observe repeating and potentially repeating FRB sources. With HyperFlash, we aim to observe the brightest and rarest FRB events by monitoring each source for hundreds to thousands of hours – predominantly around 1.3 GHz, but occasionally around 350 MHz and 5 GHz central frequencies as well. Our HyperFlash campaign on FRB 20240619D used the 25-m Westerbork RT-1 telescope (the Netherlands), the 25-m Stockert telescope (Germany), and the 25-m Dwingeloo telescope (the Netherlands). The latter two telescopes are operated primarily by amateur astronomers, on a volunteer basis. In addition, we complement the HyperFlash data by including lower-cadence observations with the much more sensitive Nançay Radio Telescope (NRT; France) – which is approximately as sensitive as a 95-m diameter radio dish. These data were acquired as part of the Extragalactic Coherent Light from Astrophysical Transients (ÉCLAT) observing programme (PI: D. M. Hewitt), which targets repeating FRBs. Since the start of 2022, ÉCLAT has been monitoring a sample of roughly 20 repeating FRB sources for about 1 hr week^{-1}, each.

2.1.1 *Westerbork RT-1*

At Westerbork, we use an FRB search pipeline that has been described most recently in O. S. Ould-Boukattine et al. (2026). We capture and store raw voltage data ('waveform data' or 'baseband data') in the `VDIF` format with dual circular polarization channels and 2-bit sampling (A. Whitney et al. 2010). Subsequently, we convert the baseband data to 8-bit total intensity (Stokes I) `SIGPROC` filterbank files using `digifil` (W. Straten & M. Bailes 2011). To mitigate dispersive smearing within frequency channels, we created filterbank files at specific time and frequency resolutions that depend on the observed radio frequency range. For observations conducted at P-band (centred at 324 MHz), we created filterbank files with a time resolution of 128 μs and a frequency resolution of 7.8125 kHz. At *L* band (1.3 GHz central frequency) we used 64 μs and 15.625 kHz resolutions, respectively. When searching the data for bursts, we excise radio frequency interference (RFI) by applying a static mask to remove known affected frequency ranges. We use `Heimdall` (B. R. Barsdell 2012) to identify burst candidates, where we set a signal-to-noise (S/N) threshold of 7 and a maximum boxcar width of 1024 (or 65 ms). To minimize the number of false positives, we only search the data within a DM range of $\pm$ 50 pc cm^{-3} around the known DM of FRB 20240619D. Initially, we searched around a DM of 480.7 pc cm^{-3} (which was reported at the time of discovery J. Tian et al. (2024)), and then later changed this to 464.87 pc cm^{-3} after we optimized the DM on our initial detection, as described in O. S. Ould-Boukattine et al. (2024). Burst candidates were automatically evaluated using the machine learning burst classifier `FETCH` (D. Agarwal et al. 2020). We specifically use models A and H, as previous testing showed they are the most reliable and consistent FETCH models (M. P. Snelders 2022), and require that at least one of the two models classifies the candidates with greater 50 per cent probability of being astrophysical in origin. Candidates are manually evaluated if either model exceeds this threshold. As an additional check, regardless of FETCH assigned probability, we also manually inspected all burst candidates that have a DM of $\pm$ 5 pc cm^{-3} around the expected DM. In total, Westerbork observed for 55.1 h at P-band and 261.3 h at L-band, with a fluence detection limit of 46.5 Jy ms and 6.6 Jy ms at P- and L-band, respectively. These limits correspond to a 7σ detection threshold. Table 2 summarises the observational setup.

2.1.2 *Stockert*

The Stockert observing and searching strategy has most recently been described in O. S. Ould-Boukattine et al. (2026). At Stockert, we record 32-bit total intensity data using the Pulsar Fast Fourier Transform (`PFFTS`) backend (E. D. Barr et al. 2013). We then convert these data into 32-bit float filterbanks using the `filterbank` tool from the `Sigproc` package. The time and frequency resolutions of the filterbanks are 218.45 μs and 586 kHz, respectively. We search for bursts using tools from the `PRESTO` package (S. Ransom 2011b). We dedisperse the data at DM$_{\rm FRB}$ = 464.87 $\pm$ 10 pc cm^{-3} using `prepsubband` and mitigate RFI by using `rfifind`. Using `single_pulse_search.py`, we search for burst candidates with a S/N threshold of 8 and consider boxcar sizes up to 300, corresponding to boxcar widths of $\sim$ 65 ms. Finally, using `FETCH`, we then classify the reported burst candidates using models A and H and a threshold of $>$ 50 per cent that the candidate is astrophysical in origin. Stockert observed a total of 142.5 h and has a fluence detection threshold of 6.4 Jy ms (Table 2).

2.1.3 *Dwingeloo*

With Dwingeloo, we simultaneously record data at both P-band (400–420 MHz) and L-band (1200–1400 MHz). At P-band, we record 32-bit filterbank data in two polarization channels (horizontal and vertical) with a time resolution of 192 μs and a frequency resolution of 0.125 MHz across 160 channels, providing a total bandwidth of 20 MHz. At *L* band, we record one channel of 32-bit filterbank (left-hand circularly polarized) data with a time resolution of 198.4 μs and a frequency resolution of 0.3125 MHz across 640 channels, for a total bandwidth of 200 MHz. Simultaneously, baseband data is recorded in a 10 min buffer, but not searched. These baseband data can be stored if a bright and interesting astrophysical event is detected in the semi-real-time filterbank search. Both the filterbank and baseband (SigMF) data are written using the `vrt-iq-tools` [1] package. The data

[1] https://github.com/tftelkamp/vrt-iq-tools

Table 2. Observational set-up.

Station[a]	Band	Frequency (MHz)	Bandwidth[b] (MHz)	Bandwidth per subband (MHz)	SEFD (Jy)	Detection[d] threshold (Jy ms)	Completeness[e] threshold (Jy ms)	Time observed[f] (h)	Time observed[g] (h)
Wb	P_{Wb}	300–356	50	8	2100[c]	46.5	172.5	–	55.1
Dw	P_{DW}	400–420	20	20	$\sim$ 2100	–	–	–	20.1
Dw	L_{Dw}	1200–1400	180	100	$\sim$ 850	–	–	–	17.3
Wb	L_{Wb}	1207–1335	100	16	420[c]	6.6	24.4	166.1	261.3
NRT	L_{NRT}	1228–1740	500	512	25	0.18	0.65	5.5	7.8
St	L_{St}	1332.5–1430.5	90	98	385	6.4	23.6	117.6	142.5
Total time at 1.4 GHz (L band) on source (hr)[g]									323.9
Total telescope time/total time on source (h)[h]									504.1/353.9

[a] Wb: Westerbork RT1, St: Stockert, Dw: Dwingeloo, NRT: Nançay radio telescope
[b] Effective bandwidth accounting for RFI and band edges.
[c] From the EVN status page.
[d] Assuming a 7σ detection threshold and a typical FRB pulse width of 1˜ms.
[e] Assuming a 15σ detection threshold and a width of 3˜ms.
[f] On-source hours between MJD 60 497 and 60 569 (6 July–16 September 2024) used for the cumulative burst energy distribution shown in Fig. 8.
[g] Total on-source hours during the full observational campaign between MJD 60 496 and 60 602 (5 July–19 October 2024).
[h] Total time on source accounts for overlap between the participating telescopes.

are searched using tools from the PRESTO package (S. Ransom 2011a). Specifically, `DDplan.py` is used to create the dedispersion plan for our filterbank files, searching within $\pm$10 per cent of the expected DM, $DM_{frb} = 480.7$ pc cm^{-3} (J. Tian et al. 2024). The DM_{frb} was only updated to the more accurately DM measurement, as described in Section 2.1.1, after the conclusion of our observational campaign. An `rfifind` mask is applied for RFI mitigation as `prepsubband` incoherently dedisperses the filterbank data. The `single_pulse_search.py` script is then used to detect pulses above a S/N threshold of 6. To reduce the number of candidates by order $\sim$ DM trials, we use DBSCAN clustering to cluster the candidates (M. Ester et al. 1996). If, after clustering, there are more than 800 candidates, the file is skipped but not deleted. A high number of candidates indicates a large amount of RFI, and the data cannot be searched in real time in such cases. However, the data are retained in case another telescope makes a detection for a potential co-detection. Candidates are classified using `FETCH` model A (D. Agarwal et al. 2020), with a detection threshold of $>$ 50 per cent probability that the candidate is astrophysical in origin. Candidates that are judged as being promising by `FETCH` are manually inspected. The full pipeline is open-source and available online.[2] Dwingeloo observed for 20.1 h at P-band and 17.3 h at L-band. The sensitivity of Dwingeloo at P-band is comparable to P-band at Westerbork with a SEFD of $\sim$2500 Jy. At L band, the SEFD is $\sim$850 Jy which is less sensitive compared to Westerbork and Stockert (See Table 2). The variable and often intense RFI environment, due to the close proximity of the telescope to the ASTRON and JIVE headquarters, can affect the effective detection threshold, leading to fluctuations in burst detectability.

2.2 Nançay Radio Telescope

The recording and custom search pipeline employed at the NRT has been described most recently in D. C. Konijn et al. (2024). At 1.4 GHz, the NRT has a system temperature of $T_{sys} \approx 35$ K and a gain of $G \approx 1.4$ K Jy^{-1}. The low-frequency receiver (1.1–1.8 GHz) of the focal plane and receiver system, *Foyer Optimisé pour le Radio Télescope*, was used to conduct the observations. The Nançay Ultimate Pulsar Processing Instrument (NUPPI; G. Desvignes et al. 2011) recorded 32-bit data with full-polarization information (in a linear basis), 16 µs time resolution, and 4 MHz frequency resolution. The 512 MHz observing bandwidth was centred at 1484 MHz, and split up into eight subbands, each divided into 16 channels. To calibrate the polarimetric data, each observation is accompanied by a 10 s observation of a 3.33 Hz pulsed noise diode. To compensate for the wide channel widths, we applied coherent dedispersion using a DM of 480.7 pc cm^{-3}, as specified in the discovery ATel (J. Tian et al. 2024). We updated the DM in our search pipeline to the best-fitting value only after the observational campaign was completed. The applied coherent DM differs by 15.84 pc cm^{-3} from the best-fitting DM reported in O. S. Ould-Boukattine et al. (2024) and used throughout the analysis of the NRT burst sample. This offset introduces intra-channel temporal smearing ranging from 100 µs in the highest-frequency channel to 283 µs in the lowest-frequency channel. The NRT carried out 9 observations for a total of 7.1 h, between 6 July 2024 and 24 October 2024, and has a fluence detection threshold of 0.18 Jy ms (Table 2).

3 ANALYSIS AND RESULTS

3.1 Burst properties

3.1.1 HyperFlash

To measure the burst properties we used `filterbank` files. Additionally, to correct for digitisation effects caused by the limited dynamic range of the 2-bit sampling in observations conducted with Westerbork, we apply the scattered power correction (SPC) algorithm to these bursts (W. Straten 2013). This technique has been demonstrated in earlier work as described in O. S. Ould-Boukattine et al. (2026) and F. Kirsten et al. (2024). Bursts detected with Stockert show no digitisation effects owing to the 32-bit recording, whereas the detection with Dwingeloo does not allow accurate burst property measurements due to strong RFI.

We correct for the dispersive delay using an optimal DM determined in cases where the bursts showed fine temporal structure ($\lesssim$ 100 µs,) also known as 'microshots', as listed in Appendix Ta-

[2] https://gitlab.camras.nl/dijkema/frbscripts/-/tree/main

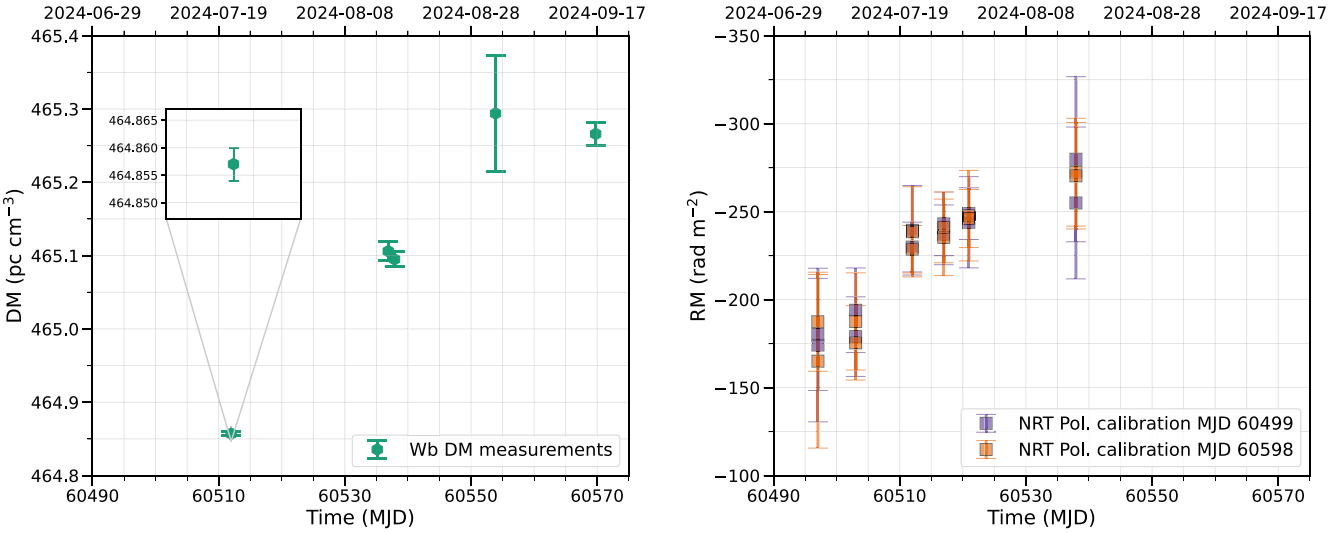

Figure 1. Left: Evolution of the DM for five bursts observed with Westerbork, plotted over time. The baseband data and presence of microstructure enabled precise DM measurements; see Fig. 2 for the corresponding dynamic spectra and S/N versus DM fitting curves. The DM varies by up to 0.41 pc cm^{-3} over a two-month span. Right: RM of ÉCLAT-detected bursts as a function of time. For each day with detections, the RM was measured for two bursts, to check for consistency. We calibrated the data using two different polarization calibration modelling (PCM) files taken on different dates. The four RM values per day are consistent with each other. We find that the absolute RM increases by ∼80 rad m^{-2} over a period of 40 d.

ble D1 and shown in the left panel of Figs 1 and 2. For bursts where a precise (ΔDM < 0.1 pc cm^{-3}), individual DM measurement was not possible, we adopt the value of 464.857 pc cm^{-3}, corresponding to the DM of the brightest burst, B01–Wb, in our sample. RFI-affected frequency channels are mitigated by manually flagging the channels using tools from the `PSRCHIVE` software package, such as `psrzap` and `pazi`. Additionally, we flag the edges of subbands due to a drop in sensitivity at these frequencies. We manually determine the start and stop times of each burst. We determine the frequency extent of each burst by computing the two-dimensional autocorrelation function (ACF) and fitting a Gaussian function to the frequency axis of the ACF. If twice the full width at half maximum (FWHM) of the Gaussian is greater than or equal to 75 per cent of the total observing bandwidth, we define the burst frequency extent to be equal to the full bandwidth. This condition was met for all bursts in the HyperFlash burst sample. We determine the fluence by summing over the frequency extent and converting the time bins to flux densities using the radiometer equation. Here we assumed a constant system equivalent flux density (SEFD) for all observations, as shown in Table 2. Finally, we determine the burst time of arrival (ToA) by fitting a Gaussian to the time profile and defining the ToA as the centre of the Gaussian. We report the ToA values as barycentric arrival times in the TDB time-scale assuming a dispersion constant of $\mathcal{D} = 1/(2.41 \times 10^{-4})$ MHz^2 pc^{-1} cm^3 s with respect to infinite frequency for the measured DM of the burst. For burst B06–Dw, detected with the Dwingeloo telescope (Fig. 3), we were only able to measure the ToA of burst, as strong RFI during the event prevents further analysis.

HyperFlash detected 11 bursts of which 3 bursts were detected by more than 1 telescope. All burst properties are listed in Appendix Table D1. The table is also available in `.csv` format as part of the supplementary material. An overview of Westerbork-detected bursts for which baseband data are available is shown in Appendix Fig. B2. All bursts are plotted at the same time and frequency resolution, but on different time-scales, highlighting the diversity in burst morphology and the presence of microstructure. Some bursts, such as B02-Wb and B10-Wb, are more than 10 ms wide, making it difficult to constrain the DM with high precision. In contrast, other bursts exhibit unresolved emission on microsecond time-scales, allowing for precise DM measurements, as discussed further in Section 3.2.

3.1.2 *ÉCLAT*

We dedispersed all the ÉCLAT-detected bursts using a single DM of 464.86 pc cm^{-3}, determined to be the optimal DM for our brightest burst (B26-NRT) which is shown in Fig. 4. We determined the burst properties using a set of interactive custom Python scripts which were specifically designed for analysis of bursts detected with the NRT. These scripts are publicly available via `GitHub`.[3] The first step is to correct the bandpass, by subtracting the mean and dividing by the standard deviation of the off-burst noise on a per-channel basis. Initial RFI flagging was done using `jess`,[4] where we flagged frequency channels with skewness outliers exceeding 3σ, after which we manually masked any remaining channels contaminated by RFI. The event duration of an individual burst and spectral extent are manually selected. This is done because many bursts have multiple subcomponents and/or are not well fit by a simple Gaussian model. The fluence is calculated by summing over the entire observing bandwidth, normalizing using off-burst noise to convert to S/N units, multiplying by the radiometer equation to convert to flux densities, and then integrating over the burst duration.

We used the Pulsar Archive Calibration program, `pac`, from the `PSRCHIVE` tools (A. W. Hotan, W. van Straten & R. N. Manchester 2004) to perform polarimetric calibration. The expected RM

[3] https://github.com/astroflash-frb/burst_analyzer
[4] https://github.com/josephwkania/jess

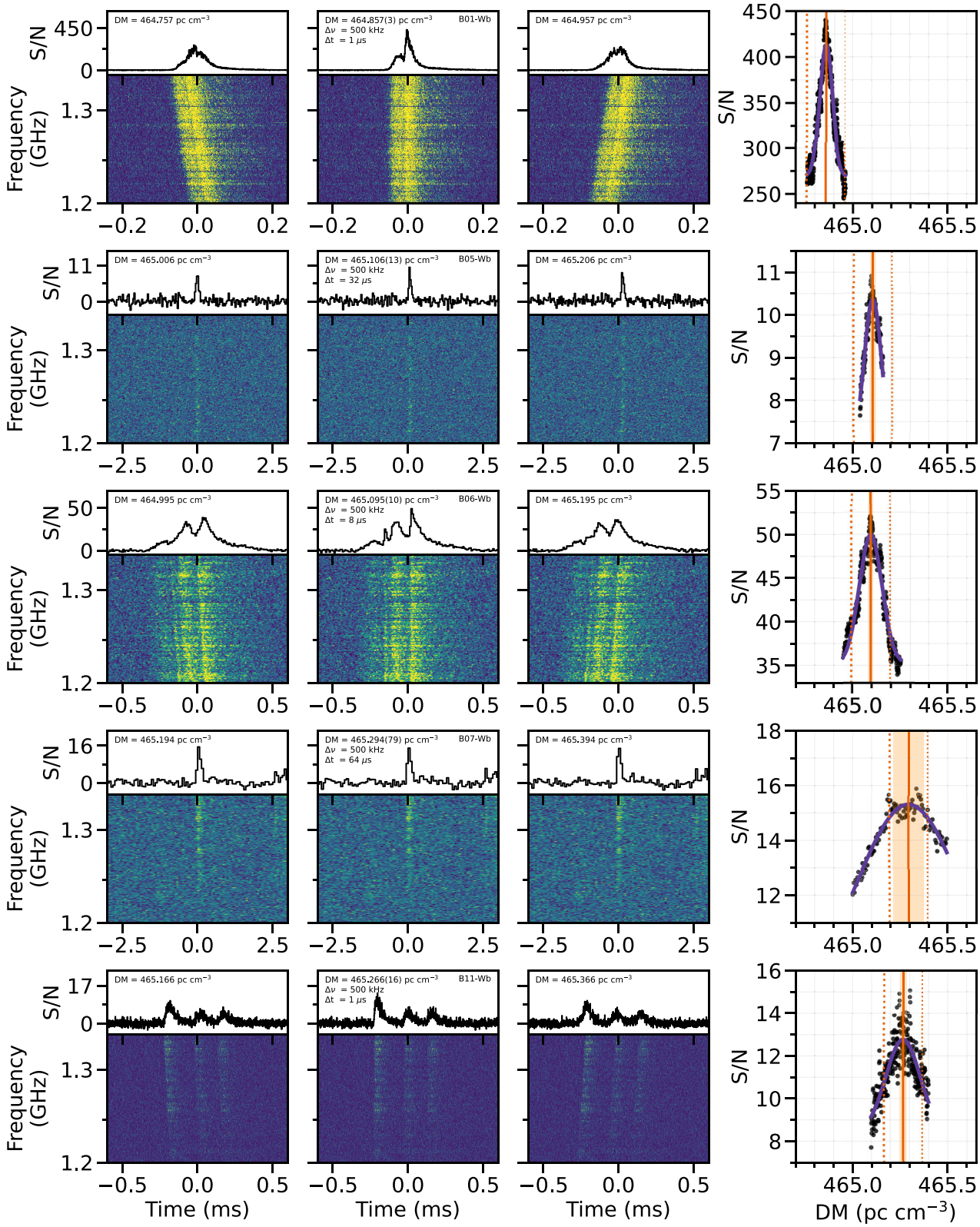

Figure 2. The dynamic spectra and time series for five bursts detected by Westerbork that show fine ($\lesssim$ 100 μs) temporal structure. A single DM value does not appropriately correct for the dispersive delay. All bursts have been coherently dedispersed to the indicated DM and we zoom in on the parts of the bursts that show fine temporal structure. The second column displays the burst spectra and time series using the S/N-optimized DM. The time and frequency resolution used for each filterbank is noted in the top panels. For illustrative purposes, The first and third columns show the bursts dedispersed to the best DM minus and plus 0.1 pc cm^{-3}, respectively. Finally, the fourth column shows the Gaussian fits to the S/N versus DM curves. The solid orange lines and the light orange regions indicate the best-fit DM and its uncertainty range. The dotted orange lines mark the $\pm$ 0.1 pc cm^{-3} values used in the first and third columns.

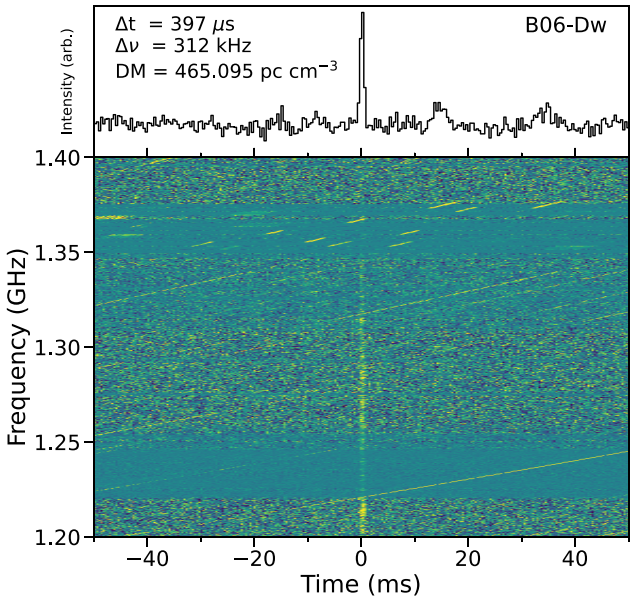

Figure 3. Burst (B06-dw) detected by Dwingeloo. Due to strong RFI in the data it was not possible to measure any burst properties accurately. The DM used is the same as for burst B06-wb as detected by Westerbork, shown in Fig. 2. This detection of this bright FRB demonstrates the observational capabilities of the Dwingeloo telescope.

of $-185\,\mathrm{rad\,m^{-2}}$ (J. Tian et al. 2025) results in the bursts exhibiting $\lesssim 2$ cycles of Faraday rotation across the observing band in Stokes Q/U, which limits the precision of our RM measurements. Therefore, for each of the six observations with detections, we select the two brightest and most broad-band bursts. We used `rmfit` from `PSRCHIVE` to search for the RM that maximizes the linearly polarized flux in a range of -1000 to $1000\,\mathrm{rad\,m^{-2}}$. The resulting Faraday Dispersion Functions (FDFs) of the 12 different bursts can be seen in Appendix Fig. C1. We find that the absolute value of the RM appears to be increasing over time. We then fit a Gaussian function to the main peaks of these FDFs, and quote the centre of the Gaussian as the derived RM value, with the FWHM of Gaussian divided by the S/N as the uncertainty on the RM. These values are also tabulated in Appendix Table D2.

Fig.4 shows the calibrated polarimetric profile of the exceptionally bright burst B26–NRT, which corresponds to the same event as B01-Wb. We additionally show both bursts side by side in Fig. 5 on the same time-scale. The linear polarisation has been unbiased and the PDF of the PPA was calculated following the formalism in J. E. Everett & J. M. Weisberg (2001). The burst is nearly 100 per cent linearly polarized, and the PPA varies by a few degrees at most across the burst duration. Upon closer inspection, the PPA exhibits slight temporal variations ($\lesssim 1^\circ$) around the time of the brightest feature in the burst. There are various factors that we can not perfectly account for that can contribute to subtle variations in the PPA. First, the temporal smearing due to the difference in DM used for incoherent and coherent dedispersion is up to 283 μs (at the lowest-observed frequencies) which is equivalent to the time-scale of the tentative PPA variations at the time of the brightest feature. The brightness of this feature also resulted in spectral leakage between channels ('spectral ghosts' are clearly visible around the bright feature). Finally, RFI is likely not perfectly excised due to the broad channels. We thus refrain from interpreting these subtle variations of less than a few degrees in the PPA.

In total, NRT detected 206 bursts. All burst properties can be found in Appendix Table D2. Additionally, this table is also available in `.csv` format as part of the supplementary material.

3.2 DM variation between bursts

Quantifying DM variation between bursts provides a means to probe the slight variations in the line of sight or the local environment of a repeating FRB source. We record the raw voltage data for Westerbork observations, which allows us to create data products with a time resolution as high as 31.25 ns. We use the Super FX Correlator (`SFXC`) to coherently dedisperse and channelise our data (A. Keimpema et al. 2015). Five of the seven bursts detected with Westerbork show structure on tens of microsecond time-scales, see Appendix Fig. B2. To optimize for the DM, we create coherently dedispersed filterbank files for a range of trial DM values, with steps of $0.001 - 0.01\,\mathrm{pc\,cm^{-3}}$ depending on the brightness and time-scale of the microstructure components. This method prevents residual smearing within a channel. For each trial DM, we then measure the peak S/N for the brightest feature of the burst. We then fit a Gaussian function to the resulting S/N versus DM curve to determine the optimal DM and its uncertainty. We were not able to constrain the DM of two bursts (B02-Wb and B10-Wb) with high accuracy ($\Delta\mathrm{DM} < 0.1\mathrm{pc\,cm^{-3}}$) due to the lack of microshots; therefore, we adopt the DM of the brightest burst (B01-Wb) for them.

In Fig. 2, we show the resulting S/N versus DM curve for five bursts. Additionally, we show the coherently dedispersed dynamic spectrum for each burst, at their 'best' value and $\pm 0.1\,\mathrm{pc\,cm^{-3}}$. The figure shows that a single DM value does not appropriately correct for the dispersive delay for all five bursts. In the left panel of Fig. 1, we show the measured DM values for each burst as a function of time. We find that DM varies between 464.857 ± 0.003 and $465.266 \pm 0.016\,\mathrm{pc\,cm^{-3}}$, which is a total change of $0.41 \pm 0.016\,\mathrm{pc\,cm^{-3}}$, over a period of approximately two months.

3.3 Apparent DM variations within a single burst

During our observing campaign, the brightest burst in our sample was simultaneously detected with Westerbork and Nançay, B01–Wb and B26–NRT, respectively (Fig. 5) (O. S. Ould-Boukattine et al. 2024). Using the Westerbork data, we precisely measured the DM to be $464.857 \pm 0.003\,\mathrm{pc\,cm^{-3}}$ (see Section 3.2). We also optimize the DM for the NRT-detected burst (Fig. 4). We dedispersed the burst over a range of trial dispersion measures and measured the peak S/N of the brightest component at each step. We then fit a Gaussian function to the resulting S/N curve to determine the optimal DM. The fit, shown in the left column of Appendix Fig. F1, yields a best-fit DM of $464.863 \pm 0.029\,\mathrm{pc\,cm^{-3}}$. This value is consistent with the aforementioned DM derived from the Westerbork data, as shown in the top row of Fig. 2.

After correcting for dispersion, we find that the burst has a component that shows an apparent residual drift, starting at ∼20 ms in the dynamic spectrum of Fig. 4. The other shorter components of this burst, occurring before and after this drifting feature, do not show any evidence for such a drift. The drifting component shows an intensity dip that is most visible in the time series. To quantify apparent drift, we optimized the DM by fitting the narrow intensity dip (right column of Appendix Fig. F1)

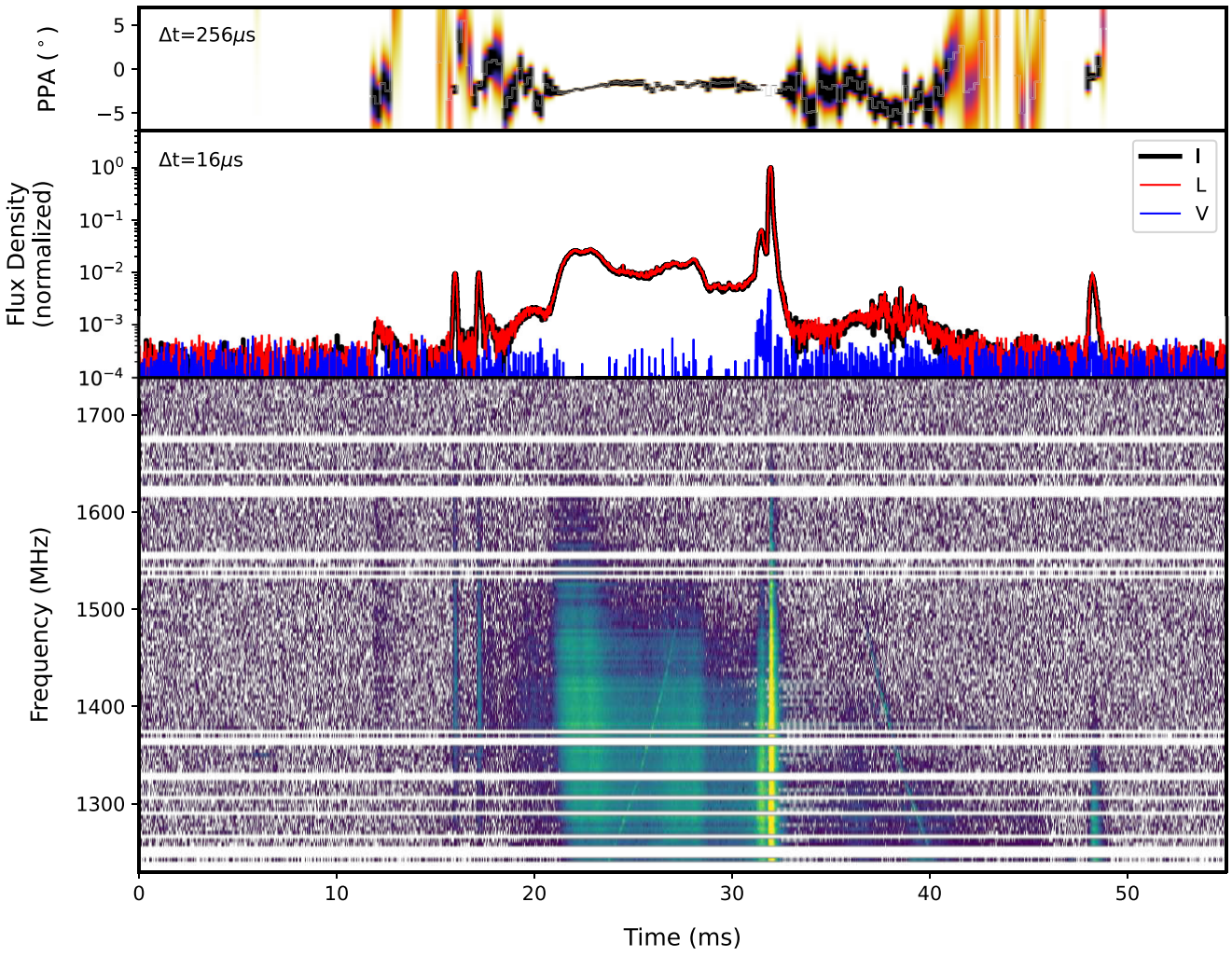

Figure 4. The bottom panel shows the dynamic spectrum of B26-NRT. The colour map is scaled logarithmically. This burst has been coherently dedispersed to a DM of 480 pc cm^{-3}, and incoherently dedispersed to a DM of 464.86 pc cm^{-3} (see Section 3.1.2). The horizontal white lines indicate channels that have been excised due to the presence of RFI. The middle panel shows the frequency-integrated burst profile in black, also on a logarithmic scale. The linear and circular polarization are shown in red and blue, respectively. The top panel shows the probability density function (for each time bin) of the PPA, which varies by less than a few degrees across the burst duration. The time resolution here has been downsampled by a factor of 16, to account for the DM smearing (283 μs in the lowest-frequency channel) due to the difference between the DM that was used for coherent dedispersion and the true DM of the burst.

with an upside down Gaussian. We find the component straightens out at a DM of 465.540 ± 0.028 pc cm^{-3}. This DM differs by $+0.677$ pc cm^{-3} compared to the DM that straightens all other sub-bursts.

3.4 Scattering analysis

Three bursts in the sample show frequency-dependent asymmetries suggestive of pulse broadening due to multipath propagation. We infer the scattering delays τ of these bursts by modelling the burst profiles as the convolution a Gaussian pulse (or series of Gaussian pulses) with a one-sided exponential that has a $1/e$ delay τ that scales with observing frequency as $\tau \propto \nu^{-4}$ (as strictly required for the assumption of a Gaussian scattered image; H. C. Lambert & B. J. Rickett 1999; A. Geiger et al. 2025). All of the bursts we consider have multiple components, which we model as the sum of N Gaussians each convolved with a one-sided exponential. The number of sub-components N included in the model is kept to the smallest number possible while minimizing χ^2. We also fix τ to be constant across all sub-components in an individual burst. To fit for τ, we evaluate the mean burst profile in multiple frequency subbands, where the number of subbands is set to yield a peak S/N $>$ 10. To reduce the number of free parameters, the mean arrival times of each sub-component are fixed across all subbands. The Gaussian amplitudes of each sub-component are allowed to vary freely between subbands, while the Gaussian widths are only allowed to vary slightly (by $<$ 20 per cent).

Fig.6 shows the best-fitting burst profiles for the three bursts with evidence of pulse broadening. We infer scattering delays $\tau_{\text{B02-Wb}} = 1.3 \pm 0.3$ ms at 1228.25 MHz, $\tau_{\text{B06-Wb}} = 75 \pm 7$ μs at 1222.75 MHz, and $\tau_{\text{B11-Wb}} = 40 \pm 7$ μs at 1313.25 MHz for these three bursts, respectively. Scaling τ to 1 GHz assuming $\tau \propto \nu^{-4}$ yields respective scattering delays $\tau_{\text{B02-Wb}}(1\text{ GHz}) = 2.9 \pm 0.7$ ms, $\tau_{\text{B06-Wb}}(1\text{ GHz}) = 170 \pm 16$ μs, and $\tau_{\text{B11-Wb}}(1\text{ GHz}) = 120 \pm 21$

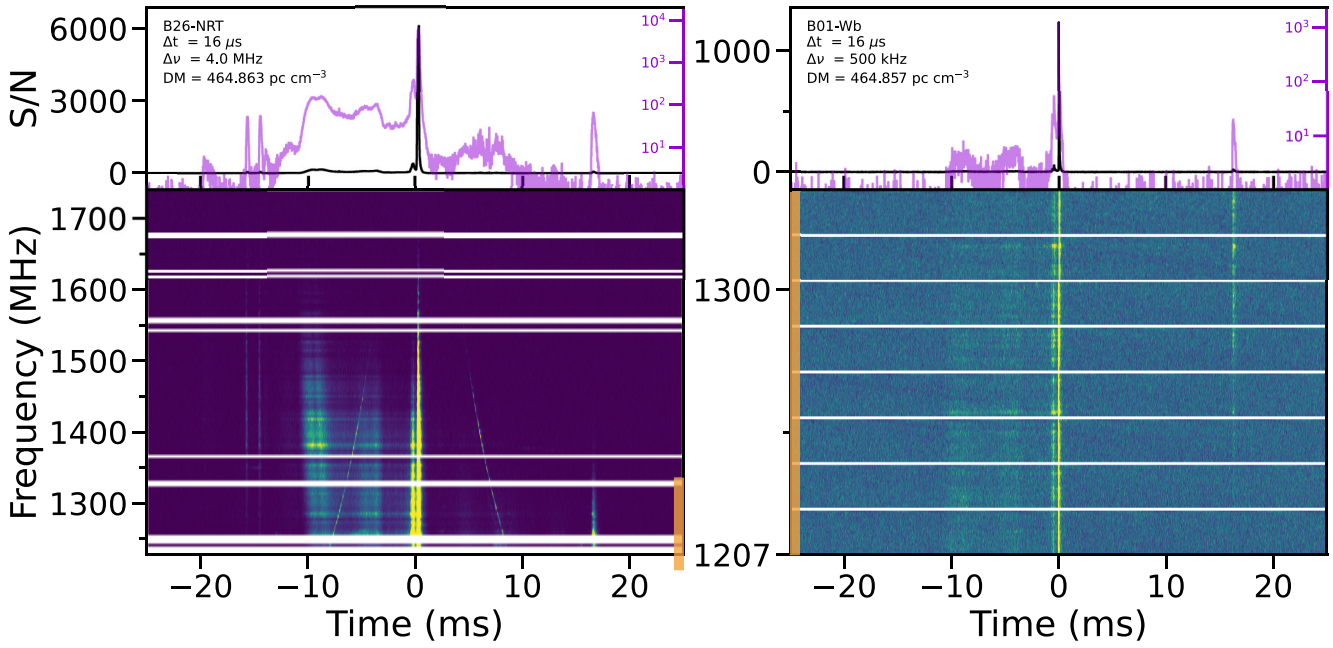

Figure 5. Time series (top panels) and dynamic spectra (bottom panels) for the brightest burst simultaneously detected by Nançay (B26–NRT) and Westerbork (B01–Wb). The orange patches indicate the 128 MHz frequency range partially overlapping between the observing setups. The top-left panels show the plotted time and frequency resolutions as well as the applied DM. B26–NRT data were only incoherently dedispersed (between channels), whereas B01–Wb data were also coherently dedispersed (within channels). Although the applied DM values differ slightly between bursts, they remain consistent within the measurement uncertainties (Figs 2 and Appendix F1). White vertical lines indicate channels zapped due to RFI or are channels at the subband edges.

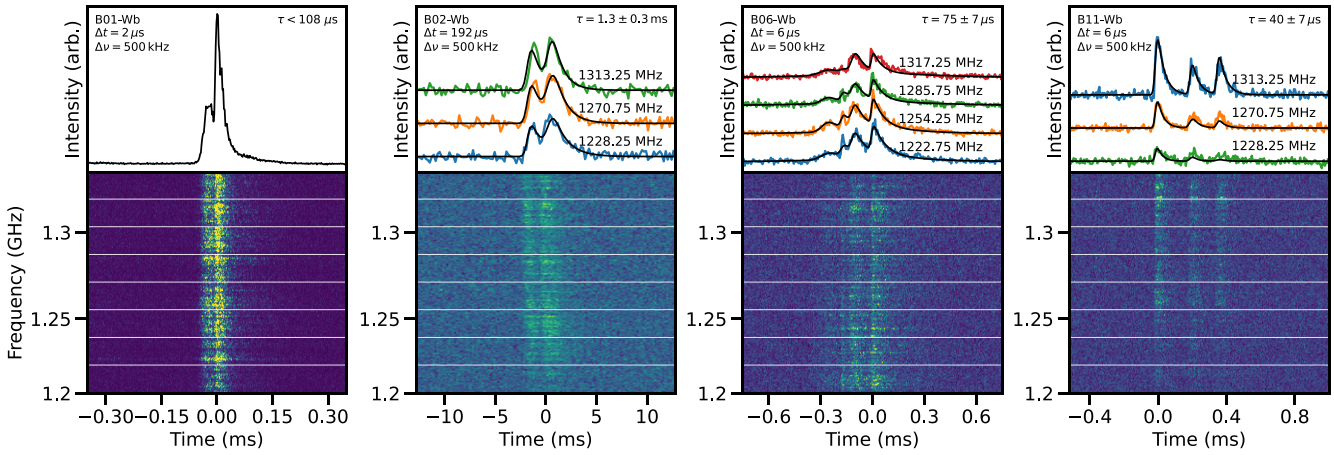

Figure 6. Pulse broadening constraints for four Westerbork bursts. Bottom panels show dynamic spectra and upper panels show frequency-averaged burst profiles. In the upper panels we also indicate the burst ID, as well as the time and frequency resolution of each burst. The three right-hand bursts show evidence of chromatic pulse broadening consistent with scattering delays τ noted on each panel; each τ is referenced to the lowest-frequency subband. Black curves show the best-fit burst models (see Section 3.4). The first burst, B01–Wb, instead provides a stringent 95 per cent confidence upper limit on the scattering delay based on the empirical width of its ACF, $\tau < 108$ μs at 1271 MHz.

μs. We note that one of these bursts (B06-Wb) is best fit by a model with five sub-components, and the 1σ error quoted on τ for this burst is likely an underestimate. Regardless, these results suggest that the scattering delay may vary significantly between bursts.

The top-left panel of Fig. 6 also shows the frequency-averaged burst profile of an extremely bright burst (B01–Wb) that does not show clear evidence of frequency-dependent pulse broadening. Evaluating the temporal ACF of this burst (following methods in S. K. Ocker et al. 2023) yields an empirical upper limit on the burst FWHM of 51 ± 28 μs, which gives a 95 per cent confidence upper limit on τ, $\tau_{\text{B01-Wb}} < 108$ μs at 1271 MHz, equivalent to $\tau_{\text{B01-Wb}} < 324$ μs at 1 GHz (assuming $\tau \propto \nu^{-4}$). This empirical upper limit is almost 10 times smaller than the largest scattering delay we infer, which lends additional evidence of scattering variability.

Table 3. Scintillation measurements for the Wb RT-1 bursts.

Burst ID (Wb)	ΔTime (μs)	ΔFreq (kHz)	Galactic $\Delta\nu_{\rm scint}$ (kHz)	Galactic m^a	Extragalactic $\Delta\nu_{\rm scint}$ (kHz)	Extragalactic m^a
B01	128	3.91	159 ± 8	0.62 ± 0.01	6.4 ± 0.7	1.05 ± 0.02
B02	4096	1.95[b]	112 ± 4	1.06 ± 0.01	–	–
B05	64	7.81	99 ± 16	1.70 ± 0.05	–	–
B06	256	1.95	91 ± 3	0.95 ± 0.01	–	–
B07	64	7.81	96 ± 16	1.40 ± 0.04	–	–
B10	4096	1.95[b]	74 ± 3	1.13 ± 0.01	–	–
B11	128	3.91	121 ± 5	1.06 ± 0.01	–	–

[a]Modulation index.
[b]Downsampled from 0.122 kHz.

3.5 Scintillation analysis

For the scattering measurements described in Section 3.4, we estimate that the corresponding scintillation bandwidth from that same scattering medium is on the order of 0.1–1 kHz. The Galactic electron density model `NE2001` (J. M. Cordes & T. J. W. Lazio 2002) estimates a ISM scintillation bandwidth of 655.7 kHz (referenced to 1.271 GHz) for this line of sight (see Table 1). Therefore, the 4 MHz frequency resolution of the NRT data is too coarse to be sensitive to the expected scintillation scales. As a result, we focus on analysing the Wb RT-1 baseband data, at sufficiently high frequency resolution. We create filterbank data from the baseband data with time and frequency resolutions depending upon the duration and morphology of the burst, as listed in Table 3. Using this data, we compute frequency spectrum ACFs, which we fit for both a single and double Lorentzian function, following the methodology outlined in K. Nimmo et al. (2025). We find an approximate ∼100 kHz frequency scale consistent across all 7 bursts that we analyse, see Table 3. While we do not see evidence for strong frequency evolution of this ∼100 kHz scale (unsurprising given that our observations are at relatively high frequencies), the consistency across all bursts leads us to rule out self-noise as the cause of this frequency scale, which would change burst to burst given the drastically different burst morphologies observed. Furthermore, we find no evidence for an equivalent frequency scale in similar analysis of the off-burst data, leading us to conclude that this scale is not an instrumental or analysis artefact. The slight burst-to-burst variations in the measured scintillation scale can be attributed to differences in burst S/N and may also be due to refractive scintillation on week-month time-scales comparable to the separation between these bursts (e.g. M. Daszuta, W. Lewandowski & J. Kijak 2013). We therefore conclude that the ∼100 kHz frequency scale can be attributed to scintillation.

For the brightest burst in our sample, B01–Wb, we measure a scintillation bandwidth of 159 ± 8 kHz and a modulation index of 0.6 (at 1.271 GHz, the centre of the observing band). A second, narrower frequency scale is also present in the ACF of this burst (Fig. 7). To explore narrower frequency scale further, we analyse bursts B01–Wb, B02–Wb, B06–Wb, B10–Wb, and B11–Wb at even higher frequency resolution, given that the burst structure and baseband data allow us to probe sub-kHz scales. We create ACFs of burst spectra at a resolution of 120 Hz (60 Hz for B01–Wb), which is roughly the inverse of the temporal width of each burst. We find a ∼kHz scale in all bursts. However, structure on the same frequency scale is evident in the off-burst data, adding doubt to the astrophysical nature of this frequency scale. B01-Wb, however, shows an additional 6.4 ± 0.9 kHz scale, with a modulation index of 1.02 ± 0.1 at 1.271 GHz. For this scale we find a hint of a shallower frequency dependence, though consistent with the $\nu^{\alpha=-4}$ evolution expected for scintillation: $\alpha = 2.3 \pm 1.4$, by dividing the burst spectrum up into 16 subbands and measuring the frequency scale in each subband independently (see appendix Fig. E1). This is consistent with the upper limit of scatter broadening we measure for B01-Wb, $\tau_{\rm B01\text{-}Wb} < 108$ μs, which implies a scintillation bandwidth $\Delta\nu_{\rm scint} \gtrsim 1.5$ kHz. We therefore attribute the 6.4 ± 0.9 kHz scale to be scintillation from a second screen along the line of sight to FRB 20240619D.

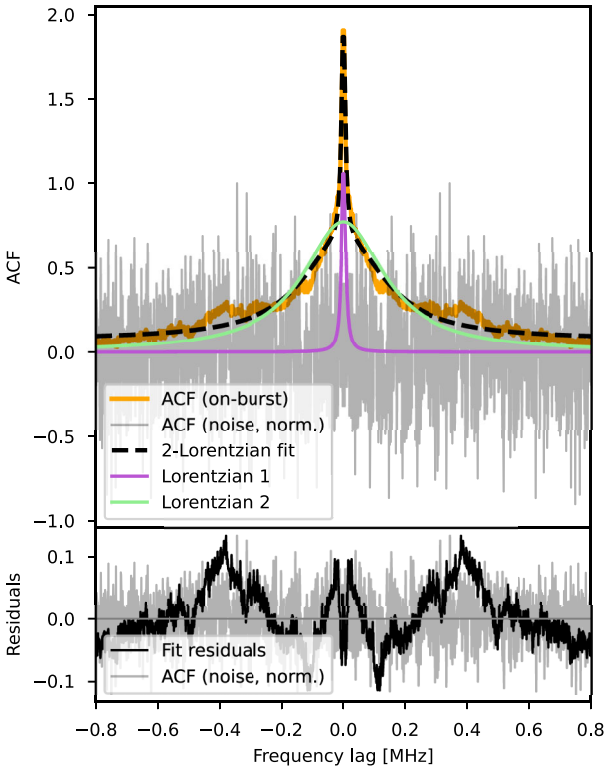

Figure 7. The autocorrelation function (ACF) of burst B01–Wb, shown in orange, using the Wb RT-1 baseband data, channelised to a resolution of 60 Hz and downsampled by a factor of 16 to 0.97 kHz. In the top panel we show the double Lorentzian fit in black, and we attribute both fitted scales to scintillation as described in Section 3.5, with the two individual Lorentzian components shown in green and purple. In the bottom panel the black line shows the residual of the double Lorentzian fit. In both panels the off-burst ACF is shown in grey and scaled to have a peak of 1 for easy comparison with the on-burst ACF.

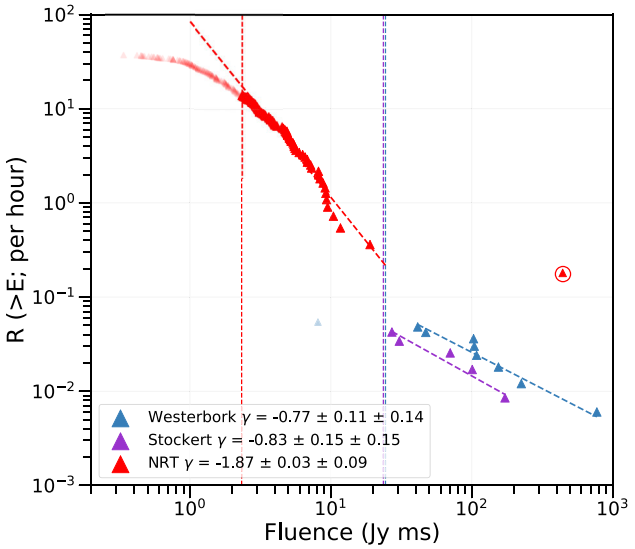

Figure 8. Cumulative burst rate distribution for Westerbork, Stockert, and Nançay (NRT) at 1.4 GHz (L band). Comparing the different rates reveals a break in the distribution towards higher energies. The burst rates are calculated based on the activity of the source between MJD 60 497 (first detection) and MJD 60 570 (last detection). The red dotted line for NRT marks the turnover point in the distribution where a single power law provides the best fit, as determined using the `powerlawPYTHON` package. The transparent data points to the left of the vertical line are excluded from the fit, as is the single circled high-energy point, which is shown only for illustrative purposes to indicate consistency with a break in the distribution. The purple and blue dotted lines represent the completeness thresholds for Stockert and Westerbork, respectively. A 20 per cent uncertainty is assumed on the burst energies. We report two error bars: the first denotes the 1σ statistical uncertainty, while the second reflects the 1-σ uncertainty derived from a bootstrapping method.

3.6 Cumulative burst rates

The cumulative distribution of burst energies can be fit using a power law, $R(>\mathcal{F}) \propto \mathcal{F}^{\gamma_C}$. Where, R is the rate of bursts, typically expressed in units per hour. $\mathcal{F}$ is the fluence of the bursts and γ_C is the slope of the cumulative distribution. In the literature, such as O. S. Ould-Boukattine et al. (2026), the burst energies are expressed in specific burst energy (erg Hz^{-1}). The specific burst energy takes account of the redshift and therefore distance to the host galaxy of the FRB. It also enables fairer comparisons between different telescopes, which often observe with different bandwidths and central frequencies. In turn, this also allows for direct comparison between different FRB repeaters. At the time of writing, there is not yet a measured redshift for FRB 20240619D. We therefore fit the power law to the cumulative distributions in terms of fluence.

We fit power laws to the cumulative burst distributions observed with NRT, Westerbork, and Stockert, as shown in Fig. 8. We restrict the analysis to the period between the first detected burst by NRT on 2024 July 6 (MJD 60497) and the last detected burst by Westerbork on 2024 September 16 (MJD 60569), in order to enable a consistent comparison of the burst rates across the different observational campaigns. The total exposure time for each telescope during this interval is listed in Table 2. To fit a power law to the distribution from Nançay, we first determine the turnover point in the distribution above which the data is best described by a single power law. We do this using the Python package `powerlaw` (J. Alstott, E. Bullmore & D. Plenz 2014). We find the turnover point to be at 2.3 Jy ms. For Westerbork and Stockert we fit a power law for bursts with energies higher than the completeness threshold. The various detection and completeness thresholds are indicated in Table 2. Next, we make an initial guess of the power-law slope (γ_C) using a maximum likelihood method, as described in D. F. Crawford, D. L. Jauncey & H. S. Murdoch (1970) and C. W. James et al. (2019). Using `scipy.optimize.curvefit`, we fit a power law and assume a 20 per cent error on the fluence values, which arises from the uncertainty in the SEFD of each telescope. We report two uncertainties in our results: the first is the 1σ error derived by `curvefit`, and the second is obtained by resampling method to assess the variance of the fit. To estimate the variance of the fit, we repeatedly draw random subsets containing 90 per cent of the bursts without replacement and refit the power law 1000 times.

We observe a break in the cumulative distribution, where the slope of Nançay is steeper than those of Westerbork and Stockert. For the fluences of Nançay, we find a steep power law of $\gamma_C^{\rm NRT} = -1.87 \pm 0.03 \pm 0.09$. We do not attempt to account for the single bright burst detected in the Nançay sample, as there are insufficient data points to fit a broken power law. Nevertheless, we include this data point in Fig. 8 for illustrative purposes, to highlight that the detection is consistent with a break in the fluence distribution. For Westerbork and Stockert, we find flatter power laws of $\gamma_C^{\rm Wb} = -0.69 \pm 0.12 \pm 0.15$ and $\gamma_C^{\rm St} = -0.83 \pm 0.15 \pm 0.16$, respectively.

4 DISCUSSION

The high sensitivity, large bandwidth and accurate polarization calibration of NRT allows for the precise determination of burst morphology and RM, while the ability to record complex voltages with Westerbork allows for the removal of intra-channel dispersion and upchannelization to precisely characterize DM and scattering/scintillation. We use the combined information from our bursts detected at the two telescopes to constrain the local environment of FRB 20240619D. We characterize the energy distribution of the source, using all bursts detected at NRT, Westerbork and Stockert.

4.1 Dispersion and rotation measure variability

By measuring the DM to high precision (order of 0.2–0.001 pc cm^{-3}) for 5 bursts, using the method explained in Section 3.2 and shown in Fig. 2, we measure an increase of the DM of + 0.41 pc cm^{-3} over two months.

Deriving accurate FRB DMs is challenging because, in the absence of microshots, dispersion and drifting effects such as downward drifting sub-bursts (the 'sad trombone' effect; J. W. T. Hessels et al. 2019; J. T. Faber et al. 2024), are difficult to disentangle. In cases with sufficient signal, one can optimize the temporal structure using a structure-optimizing algorithm such as `DM-phase` (A. Seymour, D. Michilli & Z. Pleunis 2019). However, when attempting to find the best DM for faint bursts where downward drifting is not clearly visible, it is possible to overestimate the DM. This can lead to a wide spread in measured DM values, which might be mistakenly interpreted as DM variability. None the less, accurate and precise DMs can be achieved at 1.3 GHz when an FRB displays fine temporal structure ($\lesssim 100$ μs) with high S/N. Pulsars typically show DM variability on the order of 0.001–0.01 pc cm^{-3} over timespans of months to years

(e.g. E. Petroff et al. 2013). Scaling these values naively from a ∼1 kpc pulsar line-of-sight to a typical ∼10 kpc Milky Way crossing suggests a possible Galactic contribution in these timespans of order $\lesssim 0.01$–$0.1\,\mathrm{pc\,cm^{-3}}$. These DM variations are still smaller compared to the DM variation we observe for FRB 20240619D. We therefore attribute the large DM variations reported here primarily to a turbulent local magneto-ionic environment, while noting that a small residual Galactic contribution at the level estimated above cannot be ruled out.

Long-term monitoring of repeating FRBs enables the study of the DM evolution/stability. This behaviour varies among repeaters. For example, FRB 20180916B exhibits a fairly stable DM, with three years of CHIME/FRB data showing stochastic variations of no more than $\leq 0.8\,\mathrm{pc\,cm^{-3}}$ (R. Mckinven et al. 2023a). Similarly, for FRB 20200120E, K. Nimmo et al. (2023) found that the DM remained stable within $< 0.15\,\mathrm{pc\,cm^{-3}}$ over observations spanning nearly a year. In contrast, for FRB 20121102A, D. Li et al. (2021) found that the DM varies and increases at a rate of $+0.85 \pm 0.1\,\mathrm{pc\,cm^{-3}\,yr^{-1}}$, based on a comparison of best-fit DM values from studies spanning more than seven years, between 2013 and 2020 (J. W. T. Hessels et al. 2019; L. C. Oostrum et al. 2020; J. N. Jahns et al. 2023). Following the reported increases, the DM of FRB 20121102A is now decreasing, with both P. Wang et al. (2022) ($552.5 \pm 0.9\,\mathrm{pc\,cm^{-3}}$ in September 2022) and M. P. Snelders et al. (2025) ($551.92 \pm 0.33\,\mathrm{pc\,cm^{-3}}$) reporting consistent measurements. More recently, J. Zhang et al. (2025) report a further decrease to $543.5 \pm 0.1\,\mathrm{pc\,cm^{-3}}$ in April 2025. Assuming a linear increase in the DM of FRB 20240619D with time, this corresponds to $2.46\,\mathrm{pc\,cm^{-3}\,yr^{-1}}$. This rate is approximately a factor of 3 higher than that of FRB 20121102A during the short 3 month time span over which it was observed to have an increasing DM. In contrast, the DM may not be increasing linearly on longer time-scales but could instead be fluctuating, and we may currently be observing an upward fluctuation. Both scenarios suggest that FRB 20240619D, like FRB 20121102A, is embedded in a dense magnetospheric environment.

Additionally, we measure an RM increase of $\sim 80\,\mathrm{rad\,m^{-2}}$ (> 40 per cent fractional change) for FRB 20240619D, see Section 3.1.2. Long-term monitoring of repeating FRBs also allows for the study of RM evolution and stability (R. Mckinven et al. 2023b; C. Ng et al. 2025). RM evolution is quite diverse among repeating FRBs. For FRB 20121102A, long-term monitoring revealed a ∼75 per cent decrease, from $\sim 181\,000\,\mathrm{rad\,m^{-2}}$ to $\sim 41\,000\,\mathrm{rad\,m^{-2}}$, in nearly a decade (RM values are quoted in the source rest frame, D. Michilli et al. 2018; A. Plavin et al. 2022; P. Wang et al. 2025). Likewise, FRB 20190520B shows RM variations on the order of $\sim 20\,000\,\mathrm{rad\,m^{-2}}$, including sign flips, leading to the hypothesis that the bursts are propagating through the stellar wind of a binary companion (R. Anna-Thomas et al. 2023). Aside from gradual changes, a rapid twentyfold RM increase and subsequent decrease was reported for FRB 20220529A within the span of weeks in 2023 (an 'RM flare'; Y. Li et al. 2025). These findings demonstrate the extreme local magneto-ionic environments that these sources reside in. In contrast, the hyperactive repeating source FRB 20220912A maintains a stable RM of roughly zero suggesting a less dense and/or less magnetised local environment (Y. Feng et al. 2024). Initially, the RM of FRB 20180916B has been reported to vary only stochastically by ∼3 per cent (R. Mckinven et al. 2023a), but subsequent observations from 2021 and 2022 with CHIME/FRB and LOFAR revealed a decrease in the absolute RM of $\sim 60\,\mathrm{rad\,m^{-2}}$ (∼50 per cent fractional change, R. Mckinven et al. 2023a; A. Gopinath et al. 2024). The increase of the RM of FRB 20240619D presented in this work is consistent with a subclass of repeating FRB sources that show variability in RM.

4.2 Apparent DM variability within a single burst

Evidence for DM variations within single bursts has previously been inferred from component misalignments that appear when the burst is de-dispersed using a single DM (e.g. E. Platts et al. 2021; J. T. Faber et al. 2024). Moreover, D. M. Hewitt et al. (2023) found that the microshots within larger burst envelopes were mutually consistent in DM, while some of the broader (millisecond-duration) components of the burst appeared over-dedispersed, by up to $0.3\,\mathrm{pc\,cm^{-3}}$. Nonetheless, the drifting component in B26–NRT (appendix Fig. F1) is a clear case of intra-burst DM variability. Within the context of magnetospheric models of FRB emission, we will consider two plausible explanations: multiple emission regions, or plasma lensing.

First, it is plausible that the drifting component is emitted at a lower emission height and thus becomes slightly more dispersed as it escapes the magnetosphere – though the degree of dispersion will depend on how relativistic the intervening free electrons are. Accelerated particles whose emission contributes to a single complex FRB may propagate along different magnetic field loops, which are aligned with the observer at different emission heights, resulting in slightly different dispersion measures. However, generally magnetospheric FRB emission models predict that emission closer to the surface should have a larger luminosity and higher central frequency on account of the larger magnetic field; e.g. this is true for pair production mechanisms (Z. Wadiasingh & A. Timokhin 2019), coherent curvature radiation (A. J. Cooper & R. A. M. J. Wijers 2021), and coherent inverse-Compton scattering (B. Zhang 2022). In this picture, the brighter (and narrower) burst component, which has a higher dispersion measure than the drifting component, should come from a large emission height. This is counter to most magnetospheric FRB models, disfavouring this explanation.

Secondly, the drifting component could be the result of plasma lensing of radio waves by the local ionised media within the host galaxy (J. M. Cordes et al. 2017), and possibly in the local environment. We consider this possibility, as the detected long-term RM and DM variations for FRB 20240619D (Section 4.3) imply an active, magnetised environment, which is consistent with the presence of lensing plasma in the source vicinity. As radio waves encounter a plasma lense, photons propagation along different paths with different deflection angles, θ. The total group delay then contains two frequency-dependent terms: the dispersive delay, $\tau_{\mathrm{disp}} \propto DM(\theta)\nu^{-2}$, which may vary as a function of θ due to differences in free electron density in the plasma; and a geometric delay $\tau_{\mathrm{geo}} \propto \nu^{-4}$ due to longer path length, where the frequency dependence arises due to the plasma refraction index (X. Er, Y.-P. Yang & A. Rogers 2020). A combination of these factors means plasma lensing could explain why the drifting component of the FRB accumulates a larger DM. However, R. Main et al. 2018 show in a study of giant pulses that radio emission can be amplified, by factors of a few to tens, through plasma lensing. Generically, the emission bandwidth of lensed pulses scales inversely with the magnification μ such that $\frac{\delta\nu}{\nu} \propto \mu^{-1}$ for an elongated lens (or $\propto \mu^{-1/2}$ for an elliptical lens). While the drifting component is less luminous than other burst components and appears (notwithstanding the limited observing bandwidth) to occupy a similar spectral bandwidth, it is plausible the burst

was intrinsically less luminous prior to lensing. Unfortunately, we do not record the voltage data for the NRT and the data from Westerbork lacks sensitivity and bandwidth, thereby preventing the use of the the proposed lensing tests described by Z. Kader et al. (2024). Although no definitive determination can be made, on balance it appears plasma lensing of the drifting component is consistent with our observations.

4.3 Constraining the magnetic field strength of the local environment

The coincident detection of temporal variations in DM and RM means that, under certain assumptions, the parallel magnetic field component $B_\parallel$ of the intervening material can be estimated. We take the RM changes as determined by the NRT campaign for the polarization calibration file of MJD 60598, as it shows the smallest RM variation and thus provides the most conservative magnetic field estimate (Appendix C and Extended Table D2). The NRT RM measurements span MJD 60497–60537, over which an increase in the absolute RM of $82.9 \pm 41.3\,\mathrm{rad\,m^{-2}}$ was measured. We then fit a linear slope to the three DM measurement points obtained between MJD 60511–60537 by Westerbork (Extended Table D1). Extrapolating this fit back to MJD 60497, the first epoch of the RM measurements, yields a DM value of $464.7\,\mathrm{pc\,cm^{-3}}$ (see Supplementary material). This implies a DM change of $0.38\,\mathrm{pc\,cm^{-3}}$ over MJD 60497–60537, where we neglect the subdominant DM uncertainty. Under the approximation of a uniform medium across a line-of-sight length scale such that $\int_0^L n_e(l),\mathrm{d}l = n_e L$:

$$B_{\parallel,\mathrm{mG}} = 1.23\,\mathrm{mG}\left(\frac{\Delta\mathrm{RM}}{\mathrm{rad\ \ m^{-2}}}\right)\left(\frac{\Delta\mathrm{DM}}{\mathrm{pc\ \ cm^{-3}}}\right)^{-1} \approx 0.27 \pm 0.13\,\mathrm{mG} \tag{1}$$

We note that this parallel magnetic field estimate is lower than the estimates for FRB 20121102A (0.6-2.4 mG; D. Michilli et al. 2018 and 2.2-2.6 mG; P. Wang et al. 2025), FRB 20190520B (3-6 mG; R. Anna-Thomas et al. 2023) and FRB 20190417A (> 1.3 mG; A. M. Moroianu et al. 2026). If we further assume the intervening matter is spherical, the DM variation time scale δt implies via causality an upper limit on the length scale of $L < \delta t c \approx 0.03\,\mathrm{pc} = 9.3 \times 10^{11}\,\mathrm{km}$. This corresponds to a lower limit of the number density of free electrons in the material of $n_e \gtrsim 10\,\mathrm{cm^{-3}}$ to achieve the observed δDM (e.g. $n_{e,\mathrm{min}} \sim \delta DM_{\mathrm{obs}}/L_{\mathrm{max}}$). Following D. Michilli et al. (2018), we can parametrise $B_\parallel$ in terms of the thermal particle energy at a temperature T such that:

$$B_\parallel = (\beta^{-1} 16\pi\, n_e k_B T)^{1/2} \tag{2}$$

Where $\beta = 1$ corresponds to equipartition between magnetic and particle energy densities. Using equation (2), we can express the required free electron density n_e in terms of L, β, and T. In Fig. 9, we show the constraints based on the observed RM variation for two plasma temperatures in background blue shades, which correspond to a range of $10^{-4} \leq \beta \leq 1$, where lower values of β imply higher magnetizations. The causality constraints discussed above imply that the temperature of the free electrons must be $T \lesssim 10^6$ K for $\beta = 1$, or $T \lesssim 10^2$ K for $\beta = 10^{-4}$.

There are a number of plausible scenarios to simultaneously explain the DM and RM variations. Evolving supernova remnants (SNRs) have been posited to explain the RM and DM variations of some repeating FRBs (e.g. Y.-P. Yang & B. Zhang 2017). While in late-time Sedov–Taylor phases increasing DM is predicted (A. L. Piro & B. M. Gaensler 2018), there is no prediction for an absolute RM increase. Furthermore, typical SNR length scales in this phase are larger than our inferred size constraints and should be slowly evolving, which is not supported by our observations.

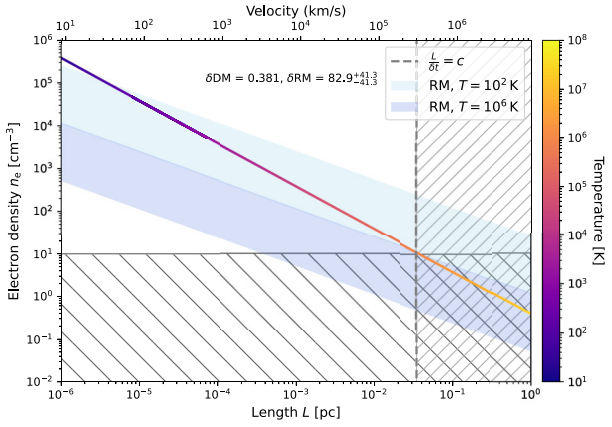

Figure 9. Constraints on the intervening matter using measured values of δDM and δRM via equation (2). The coloured line, and corresponding colour bar, denotes the required electron density n_e as a function of its longitudinal length scale L, coloured by the plasma temperature assuming equipartition (e.g. $\beta = 1$). Background shades consider a wider allowed parameter space of $10^{-4} \leq \beta \leq 1$ for $T = 10^2$ K (lighter shade) and $T = 10^6$ K (darker shade). Cross-hatched areas correspond to intervening material velocities greater than the speed of light, assuming spherical geometry and $L \sim c\delta t$ where δt is the observed time-scale of RM and DM variations.

Crab-like filaments have typical densities ($n_e \sim 10^3\,\mathrm{cm^{-3}}$; T. Temim et al. 2024) and typical widths ($L \sim 10^{-4}$-10^{-2} pc; e.g. J. J. Hester 2008) consistent with the allowed parameter space. Moreover, recent low-frequency radio observations (M. Arias et al. 2025) identified more diffuse envelopes with densities $n_e \sim 10^2\,\mathrm{cm^{-3}}$ and typical widths of $L \sim 10^{-2} - 10^{-1}$ pc, also compatible with our constraints. However, while the magnitude of RM and DM changes could be explained, it is not clear that the velocities required to produce the rate of change are compatible with Crab-like filaments. Typical turbulent velocities of $v \sim 10^2\,\mathrm{km\,s^{-1}}$ (V. Trimble 1971) appear incompatible with observations, and may required some fine-tuning: e.g. an observer aligned with non-uniform edge of a turbulent filament.

It has been suggested that some active repeaters may be magnetars in binary systems (K. Ioka & B. Zhang 2020; F. Y. Wang et al. 2022; B. Zhang & R.-C. Hu 2025). The properties of a dense (possibly clumpy), warm, and magnetized stellar wind from a massive star are consistent with the constraints presented in Fig. 9 (see also predictions in K. M. Rajwade & J. van den Eijnden 2023), and do not require large departures from equipartition.

Overall, the changing RM and DM appear to be best fit by either a clumpy stellar wind, or possibly filamentary structures surrounding the FRB source. Such structures may also give rise to the conditions required for plasma lensing discussed in Section 4.2.

4.4 Scintillation and scattering

Our scattering analysis lends further evidence that there is a dense, variable magneto-ionic environment around the source. We find evidence for two distinct scattering media (hereafter

'screens') along the line of sight. One screen produces a ∼100-kHz scintillation scale seen in seven out of nine of the bursts that were bright enough for the analysis. Given that pulsar observations indicate a spread of ≈ 0.8 dex in Galactic scintillation bandwidths and pulse broadening times for a given DM (M. A. Krishnakumar et al. 2015; J. M. Cordes, S. K. Ocker & S. Chatterjee 2022), we conclude that this ∼ 100 kHz scale is consistent with the the ≈ 660 kHz scale expected from the Milky Way foreground in this direction (J. M. Cordes & T. J. W. Lazio 2002).

We additionally infer pulse broadening delays ranging between 120 μs and 3 ms at 1 GHz. This level of pulse broadening is significantly larger than the level of scattering induced as ∼100 kHz-scale scintillation, and we attribute it to an extragalactic screen. The detection of two scintillation scales, $\Delta\nu_{\rm d} = 156$ kHz and $\Delta\nu_{\rm d} = 6.4$ kHz at 1271 MHz, in burst B01–Wb (the brightest burst in our sample) further supports this conclusion. The extragalactic scintillation scale of $\Delta\nu_{\rm d} = 6.4$ kHz corresponds to a scattering delay of $\tau \approx 1/(2\pi\ 6.4\,{\rm kHz}) \approx 24$ μs at 1271 MHz and is consistent with the inferred upper limit on the scattering delay of $\tau_{\rm B01\text{-}Wb} = 108$ μs (See Fig. 6). In this burst, the inferred modulation index $m \approx 0.6$ of the Galactic ∼100-kHz scale suggests that extragalactic pulse broadening suppresses the Galactic scintillation.

The extragalactic scattering appears to vary significantly between bursts, supporting an origin close to the source. Based on both the pulse broadening measurements and the $\Delta\nu_{\rm d} \approx 6.4$ kHz measurement in B01–Wb, we infer scattering delays that vary by at least a factor of 2, and up to a factor of 9, between bursts. This level of variability is far too large to be attributable to refractive scattering in the host ISM (e.g. Galactic pulsars show scattering delays that vary by ∼10 per cent on months-long time-scales; J. Singha et al. 2024; A. Geiger et al. 2025). Adopting the same line of reasoning applied to the DM and RM variations suggests that the scattering variations occur on length scales $\delta t c < 4 \times 10^{11}$ km (for $\delta t \approx 15$ d between bursts B01–Wb and B02–Wb).

While this FRB currently lacks a known host galaxy, we can further attempt to constrain the position of the extragalactic scattering screen based on the DM budget. We first adopt a conservative upper limit on the source redshift based on its DM, which gives $z < 0.6$ (95 per cent confidence, L. Connor et al. 2025), or $D_{\rm s} < 1.4$ Gpc (Planck Collaboration VI 2020). Based on the detection of both extragalactic pulse broadening and Galactic scintillation, we find an upper limit on the product $L_X L_G$, where L_X is the distance between the source and extragalactic screen, and L_G is the distance between the observer and Galactic screen, following methods laid out in J. M. Cordes & S. Chatterjee (2019). For the smallest extragalactic scattering delay, in burst B01-Wb ($\tau \approx 24$ μs at 1271 MHz), we find $L_X L_G < 2 \times 10^3$ kpc^2.

Adopting the largest measured scattering delay ($\tau \approx 1.3$ ms at 1228 MHz) yields a significantly smaller upper limit, $L_X L_G < 42$ kpc^2. For typical Galactic screen separations $L_G \sim 1$ kpc, both of these upper limits accommodate a screen within the host galaxy, although we emphasize that these upper limits are extremely conservative due to the unknown source redshift. Adopting the much smaller redshift upper limit inferred from the energy distribution (see Section 4.6), $z \lesssim 0.24$, yields an even smaller range $L_X L_G \sim$ 14-660 kpc^2. Future identification of the host galaxy and source redshift will yield more stringent constraints on L_X, providing an independent test of the link between scattering and the circum-source medium, as well as enabling constraints on the emission region size (K. Nimmo et al. 2025).

The scattering variability reported here is highly reminiscent of the scattering behaviour of FRB 20190520B (S. K. Ocker et al. 2023), as well as scattering variations seen in the Crab pulsar (A. G. Lyne & D. J. Thorne 1975; D. C. Backer, T. Wong & J. Valanju 2000; J. W. McKee et al. 2018) and the Galactic Centre magnetar (L. G. Spitler et al. 2014; A. B. Pearlman et al. 2018). All of these other sources are known or inferred to reside in regions of highly inhomogeneous and filamentary plasma; both the Crab pulsar and Galactic Centre magnetar are young sources that are viewed through their natal circum-source material. Similar to FRB 20190520B, we find no clear evidence of a correlation between the DM/RM and τ variations, suggesting that these propagation effects arise from different (but potentially overlapping) regions of the circum-source environment. For FRB 20190520B, the time-scale of the scattering variations is significantly faster than that of the DM and RM variations, potentially because the scattering arises from plasma inhomogeneities closer to the source (S. K. Ocker et al. 2023). For FRB 20240619D, we are unable to distinguish between the time-scales of the DM, RM, and scattering variations. Given that scattering arises from sub-au scale plasma density fluctuations, it is possible that the scattering we observe traces plasma fluctuations at much smaller spatial scales within the same evolving structure responsible for the secular change in DM and RM. The evidence for plasma lensing within a single burst, discussed in Section 4.2, hints at a similar scenario. Indeed in the Crab pulsar, plasma lensing and variability in the pulse broadening delay are empirically connected (D. C. Backer et al. 2000; A. G. Lyne, R. S. Pritchard & F. Graham-Smith 2001; T. Serafin Nadeau et al. 2024). With enough burst detections, future studies of FRB 20240619D may be able to draw similar connections between plasma lensing, pulse broadening variations, and underlying circum-stellar medium plasma properties (e.g. δn_e, size scale).

4.5 The burst fluence distribution

We fit separate power laws to the fluence distributions observed with NRT, Westerbork, and Stockert. The different slopes of these power-law fits suggest a break at approximately ∼25 Jy ms in the cumulative fluence distribution, where the distribution flattens from a steeper power law with index $\gamma \sim -1.9$ to a flatter power law beyond the break with index $\gamma \sim -0.8$. We note that the burst rate observed with Stockert is lower than that measured with Westerbork. This difference can be attributed to the fact that the two telescopes did not observe strictly contemporaneously, and that Westerbork obtained nearly one and a half times more the total exposure during the activity window (see Appendix Fig. B1 and Table 2). Additionally, FRB repeaters are known to exhibit highly variable burst rates during periods of activity, which makes it challenging to observe consistent rates in non-simultaneous observations (e.g. D. C. Konijn et al. 2024). Nevertheless, both telescopes accumulated sufficient exposure during the period in which FRB 20240619D was active to probe and observe the flat tail of the cumulative distribution. The observation of a break in the distribution towards higher energies is not unique and has been found before in other very active repeaters, such as FRB 20201124A described by F. Kirsten et al. (2024) and for FRB 20220912A by O. S. Ould-Boukattine et al. (2026). In addition, Y.-X. Huang et al. (2025) reported a tentative break in the cumulative energy distribution for FRB 20240114A, D. M. Hewitt et al. (2022) for FRB 20121102A and S. B. Zhang et al. (2024) found a single outlier in the energy distribution for FRB 20200120E.

In Fig. 8, we highlight the brightest detection with NRT (B26–NRT) using a red circle (Fig. 4). This burst was also detected using Westerbork (B01–Wb), see Fig. 5. We note that the inferred fluences of the bursts differ by a factor of 1.75, with 771 Jy ms for B01-Wb and 441 Jy ms for B26–NRT. This difference arises because the observing bands of Westerbork and NRT only partially overlap, specifically towards the bottom of the band where the brightness of the spectra of the burst is increasing. The bottom of the NRT band is at 1228 MHz, while Westerbork observes down to 1207 MHz. The bright NRT detection deviates from the main, steeper distribution fitted for NRT and appears to align more closely with the flatter distributions fitted for Westerbork and Stockert. We do not attempt to fit a broken power law based on this single outlier. Nevertheless, this suggests that with more observations and exposure hours, NRT could have probed the flattening of the high-energy tail, as it did during a longer observing campaign on FRB 20220912A (O. S. Ould-Boukattine et al. 2026).

The detection of a break in the cumulative burst fluence distribution for FRB 20240619D marks the fourth such measurement reported in the literature. This strengthens the evidence that a break in the energy distribution is a common feature of hyperactive repeating FRB sources. Bursts that deviate from the steep ($\gamma \sim -2.0$) power law occur roughly every 20–100 h (F. Kirsten et al. 2024; Y.-X. Huang et al. 2025; O. S. Ould-Boukattine et al. 2026), although this occurrence rate depends heavily on repeater activity, which is known to vary significantly with time, radio frequency, and between sources (H. Xu et al. 2022; D. C. Konijn et al. 2024). Detecting a break towards higher energies therefore requires hundreds to thousands of hours of exposure using an instrument with a completion threshold lower than ∼20 Jy ms. For hyperactive repeaters, the high burst rate facilitates the detection of the brightest events and enables probing the high-energy tail of the distribution.

In our previous work, we placed a limit on the maximum energetics of FRB 20220912A (O. S. Ould-Boukattine et al. 2026). In this work, we are not able to place a similar constraint because our sample contains too few burst detections. Although FRB 20240619D appears to have been sufficiently hyperactive (A. Kumar et al. 2024; J. Tian et al. 2025) to probe the high-energy tail, the low elevation of the source, as seen from the Northern Hemisphere, limited our observing time to a maximum of 3 h per day when the source was above an elevation of 10°. Until now, most hyperactive FRB sources have been detected by the CHIME/FRB telescope (CHIME/FRB Collabortion 2021; R. McKinven & CHIME/FRB Collaboration 2022; K. Shin & CHIME/FRB Collaboration 2024). These sources are located at high declinations making them excellent targets for high-cadence monitoring using the HyperFlash project. FRB 20240619D represents the first hyperactive source detected and located by the MeerKAT telescope. Current and future observational surveys of the southern sky could detect a new hyperactive repeaters. Obtaining hundreds to thousands of hours of exposure on these future hyperactive repeaters would then require a HyperFlash-like project utilizing telescopes located in the Southern Hemisphere.

4.6 Constraining the redshift of FRB 20240619D

Currently, FRB 20240619D has no identified host galaxy or measured redshift. In Section 4.4, we adopted a conservative redshift estimate of $z < 0.6$ (L. Connor et al. 2025), but we can constrain the redshift more tightly. To do so, we employ two independent methods. The first makes use of the Macquart ($\mathrm{DM_{IGM}}$ z) relation (J. P. Macquart et al. 2020) under conservative yet realistic assumptions, while the second, novel method relies on the observed break in the cumulative energy distribution.

First, we derive a distribution for the smooth intergalactic medium contribution ($\mathrm{DM_{IGM}}$) by decomposing the observed DM of FRB 20240619D, $\mathrm{DM_{obs}} = 464.857\,\mathrm{pc\,cm^{-3}}$, into its constituent parts:

$$\mathrm{DM_{obs}} = \mathrm{DM_{MW}} + \mathrm{DM_{IGM}}(z) + \sum_i \frac{\mathrm{DM_{halo},}_i}{1+z_i} + \frac{\mathrm{DM_{host}}}{1+z}, \tag{3}$$

Where $\mathrm{DM_{MW}}$ is the Galactic contribution (including the disc and halo); the contributions of intervening halos $\mathrm{DM_{halo,}}_i$ are summed over; and $\mathrm{DM_{host}}$ represents the contribution from the host galaxy and local environment in the source rest frame. The MW disc contribution can be estimated using the YMW16 and NE2001 electron density models (J. M. Cordes & T. J. W. Lazio 2002; J. M. Yao et al. 2017; S. K. Ocker & J. M. Cordes 2024). For the FRB's Galactic coordinates $(l, b) = (15.4559°, -23.3294°)$, we find for the YMW16 model $\mathrm{DM_{MW,disc}} = 62.7\,\mathrm{pc\,cm^{-3}}$ while NE2001 predicts $\mathrm{DM_{MW,disc}} = 94.3\,\mathrm{pc\,cm^{-3}}$. To be more conservative, we adopt a uniform prior centred on the lower estimate from YMW16, $\mathrm{DM_{MW,disc}} \sim \mathcal{U}(62.7 \pm 0.2\,\mathrm{DM_{MW,disc}})$ $\mathrm{pc\,cm^{-3}}$. The MW halo component is less certain; based on recent constraints on the circum-galactic medium (A. M. Cook et al. 2023) we assume $\mathrm{DM_{MW,halo}} \sim \mathcal{U}(10, 111)\,\mathrm{pc\,cm^{-3}}$. Combining these components, we obtain a total MW contribution of $\mathrm{DM_{MW}} = \mathrm{DM_{MW,disc}} + \mathrm{DM_{MW,halo}}$. Since the redshift is unknown, we assume a conservative $\mathrm{DM_{halo}}$ contribution of $5\,\mathrm{pc\,cm^{-3}}$ from surveys of intervening halos, e.g. S. Simha et al. (2023); for the host contribution, we assume a fixed value of $\mathrm{DM_{host}} \approx 50\,\mathrm{pc\,cm^{-3}}$ (W. R. Arcus et al. 2021). Following the formalism of J. P. Macquart et al. (2020), the mean IGM contribution is:

$$\mathrm{DM_{IGM}} = \frac{3cH_0\Omega_b f_{\mathrm{IGM}}}{8\pi G m_p} \int_0^z \frac{f_e(z')(1+z')}{E(z')}\,dz', \tag{4}$$

where $H_0 = 67.4\,\mathrm{km\,s^{-1}\,Mpc^{-1}}$, $\Omega_b = 0.049$, $f_{\mathrm{IGM}} = 0.85$ and $f_e(z') \approx 7/8$ (Planck Collaboration VI 2020; C. H. Niu et al. 2022). Rearranging this to solve for z, we place a 90 per cent confidence upper limit of $z < 0.37$.

A flattening in the cumulative energy distribution in the high-energy tail has been observed for multiple repeating FRB sources, see Section 4.5). The observed flattening in the energy distribution was enabled by high source activity combined with ample observing time, ranging from hundreds to thousands of hours. If the break in the cumulative energy distribution is a universal feature of repeating sources, similarly long exposures on sufficiently active sources should allow probing of the high-energy tail. Suppose this break consistently occurs at a characteristic energy scale across different repeaters, then it could serve as a rough distance indicator, effectively functioning as a pseudo-standard candle. By rewriting the energy function from J. P. Macquart & R. Ekers (2018), we find:

$$\frac{D_{\mathrm{L}}^2}{(1+z)^2} = \frac{E_{\mathrm{break}}}{4\pi\,\mathcal{F}_{\mathrm{break}}} \tag{5}$$

Here E_{break} is the shared breakpoint in the energy distribution of repeating sources in erg $\mathrm{Hz^{-1}}$, and $\mathcal{F}_{\mathrm{break}}$ is the breakpoint in fluence in Jy ms. D_{L}^2 is the luminosity distance and z the redshift. This expression can be numerically solved if one assumes a shared breakpoint in E_{break} and a measured breakpoint in $\mathcal{F}_{\mathrm{break}}$.

Table 4. Energy breaks for different repeaters.

Source	E-break (erg Hz^{-1})	F-break (Jy ms^{-1})	Reference
FRB 20201124A	$5.0 - 8.0 \times 10^{30}$	24–39	F. Kirsten et al. (2024)
FRB 20220912A	3.2×10^{30}	24	O. S. Ould-Boukattine et al. (2026)
FRB 20240114A	$1.0 - 2.5 \times 10^{31}$	30–73	Y.-X. Huang et al. (2025)
FRB 20240619D	-	~ 25	This work

For FRB 20240619D we observe a break in the cumulative energy distribution at 25 Jy ms (see Fig. 8). The energy distributions for various repeaters flatten in the range of 24–73 Jy ms, which corresponds to 5–25 $\times$ 10^{30} erg Hz^{-1} when converting to specific energy (erg Hz^{-1}). We take a conservative margin on these values, 1 to 30 $\times$ 10^{30} erg Hz^{-1}, and use these as lower and upper bounds for $E_{\rm break}$. We next numerically solve equation (5) and estimate the redshift of FRB 20240619D to be $z = 0.042$–0.240 (Supplementary material).

We find that the 90 per cent confidence upper limit from the Macquart (DM$_{\rm IGM}$ z) relation, $z < 0.37$, is consistent with our estimate of $z = 0.042$–0.240, which is based on the assumption that the break in the energy distribution is a common feature among repeating FRB sources (Table 4. A future host galaxy association of FRB 20240619D and a measurement of the corresponding redshift will provide a direct test of this prediction.

5 CONCLUSIONS

We conducted a high-cadence observing campaign targeting FRB 20240619D using the HyperFlash (Westerbork, Dwingeloo and Stockert telescopes) and ÉCLAT (Nançay Radio Telescope) monitoring programs. In total, we obtained more than 500 h of observations over a 4-month period and detected 217 bursts, including 10 bursts with fluences exceeding 25 Jy ms. Our main conclusions can be summarized as follows:

(i) We find burst-to-burst DM and RM variations, up to 0.41 pc cm^{-3} over 2 months and 80 rad m^{-2} over 40 d, respectively (Table 1 and Fig. 1). We detect DM variations using coherently dedispersed Westerbork voltage data that reveal short temporal features ($\lesssim 100$ μs). RM variations are detectable using the large bandwidth and accurate polarization calibration of NRT.

(ii) In addition to DM variations between bursts, we also detect apparent intra-burst DM variability between sub-bursts in the brightest burst of our sample (B26–NRT; Fig. 4). We argue that this drifting component could be the result of plasma lensing in the source's local environment or variable emission heights (Section 4.2).

(iii) Using the observed variation in DM and RM we measure the parallel magnetic field strength of the local environment, $B_{\parallel} = 0.27 \pm 0.13$ mG. This value is an order of magnitude lower compared to measurements of FRB 20121102A (0.6–2.4 mG), FRB 20190520B (3–6 mG) and FRB 20190417A (> 1.3 mG), but represents one of the few cases where a direct estimate of $B_{\parallel}$ is possible.

(iv) We also use the Westerbork voltage data to measure the scintillation bandwidth and scattering time-scales for 7 bursts (Figs 7 and 6 and Table 3). We find find evidence for two distinct screens along the line of sight. The first screen is detectable for multiple bursts and produces ∼100 kHz scintillation scales and is associated with the Milky Way. The second screen was found for a bright single burst (B01–Wb) and has a scintillation bandwidth of 6.8 kHz and is most likely located in the host galaxy or local environment of FRB 20240619D.

(v) The (time-variable) propagation effects observed towards FRB 20240619D demonstrate that it resides in a dense magnetospheric environment similar to FRB 20121102A and FRB 20190520B, but likely less extreme. Furthermore, we suggest that the observed changes in RM and DM could result due to a clumpy stellar wind from a binary companion or filamentary structures surrounding the host, which may also explain the origin of the hypothesised intra-burst plasma lensing.

(vi) We observe a break in the cumulative fluence distribution at ∼25 Jy ms (Fig. 8). Breaks in the energy distributions of repeating FRB sources have previously been found and described for FRB 20201124A (F. Kirsten et al. 2024), FRB 20220912A (O. S. Ould-Boukattine et al. 2026) and FRB 20240114A (Y.-X. Huang et al. 2025). Our detection of a break in the cumulative energy distribution of FRB 20240619D further supports the conclusion that this behaviour is common to repeating FRB sources in general.

(vii) We place a 90 per cent confidence upper limit of $z < 0.37$ based on the Macquart (DM$_{\rm IGM}$-z) relation. Additionally, assuming that the break in the energy distribution is a universal feature among repeaters, and occurs around the same characteristic energy range of 1–30 $\times$ 10^{30} erg Hz^{-1}, we estimate a redshift of $z = 0.042$–0.240. These limits and estimates are consistent. A future host galaxy association and redshift determination of FRB 20240619D will provide a direct test of these constraints.

The HyperFlash and ÉCLAT monitoring campaigns will continue observing both known and newly discovered FRB sources, for hundreds to thousands of hours per year, enabling deeper insight into burst energetics and long-term variability of propagation effects.

ACKNOWLEDGEMENTS

We thank Reshma Anna-Thomas, Amanda Cook, Jakob Faber and Jacco Vink for insightful discussions. We thank the directors and staff of the participating telescopes for allowing us to observe with their facilities. The AstroFlash research group at McGill University, University of Amsterdam, ASTRON, and JIVE is supported by: a Canada Excellence Research Chair in Transient Astrophysics (CERC-2022-00009); the European Research Council (ERC) under the European Union's Horizon 2020 research and innovation programme ('EuroFlash'; grant agreement no. 101098079); and an NWO-Vici grant ('AstroFlash'; VI.C.192.045). AJC acknowledges support from the Oxford Hintze Centre for Astrophysical Surveys which is funded through generous support from the Hintze Family Charitable Foundation. S.K.O. is supported by the Brinson Foundation through the Brinson Prize Fellowship Program, and is a member of the NANOGrav Physics Frontiers Center (NSF award PHY-2020265). KN is an MIT Kavli Fellow. ZP is supported by an NWO Veni fellowship (VI.Veni.222.295). We express our gratitude to the operators and

observers of the Astropeiler Stockert telescope: Thomas Buchsteiner, Elke Fischer and Hans-Peter Löge. This work makes use of data from the Westerbork Synthesis Radio Telescope and the Dwingeloo Radio Telescope, both owned by ASTRON. ASTRON, the Netherlands Institute for Radio Astronomy, is an institute of the Dutch Scientific Research Council NWO (Nederlandse Oranisatie voor Wetenschappelijk Onderzoek). We thank the Westerbork operators Richard Blaauw, Jurjen Sluman and Henk Mulder for scheduling and supporting observations. We express our gratitude to all volunteers running the Dwingeloo Radio Telescope. The Nançay Radio Observatory is operated by the Paris Observatory, associated with the French *Centre National de la Recherche Scientifique* (CNRS). We acknowledge financial support from the *Programme National de Cosmologie et Galaxies* (PNCG) and *Programme National Hautes Energies* (PNHE) of INSU, CNRS, France.

DATA AVAILABILITY

The data that support the plots within this paper and other findings of this study are available under https://doi.org/10.5281/zenodo.18184163 or from the corresponding author upon reasonable request. The scripts and Jupyter notebooks used to analyse the data, generate the plots and tables with the burst properties are available at https://github.com/astroflash-frb/frb20240619d-ouldboukattine-2026.

This work made use of the following software packages: `astropy` (Astropy Collaboration 2013, 2018, 2022), `Jupyter` (F. Perez & B. E. Granger 2007; T. Kluyver et al. 2016), `matplotlib` (J. D. Hunter 2007), `numpy` (C. R. Harris et al. 2020), `pandas` (W. McKinney 2010; The pandas development team 2025), `python` (G. Van Rossum & F. L. Drake 2009), `scipy` (P. Virtanen et al. 2020; R. Gommers et al. 2025), and `tqdm` (C. Costa-Luis et al. 2024). This research has made use of NASA's Astrophysics Data System. Software citation information aggregated using `The Software Citation Station` (T. Wagg & F. S. Broekgaarden 2024; T. Wagg, F. Broekgaarden & K. Gültekin 2024).

The FRB software pipeline written to process and search the baseband data can be found at https://github.com/pharaofranz/frb-baseband. `jive5ab` can be found on https://github.com/jive-vlbi/jive5ab, `Heimdall` is hosted at https://sourceforge.net/projects/heimdall-astro/ and `FETCH` can be found at https://github.com/devanshkv/fetch. The pulsar package `DSPSR` is hosted at https://sourceforge.net/projects/dspsr/ and `SIGPROC` can be retrieved from https://github.com/SixByNine/sigproc.

REFERENCES

Agarwal D., Aggarwal K., Burke-Spolaor S., Lorimer D. R., Garver-Daniels N., 2020, MNRAS, 497, 1661
Alstott J., Bullmore E., Plenz D., 2014, PLoS ONE, 9, e85777
Anna-Thomas R. et al., 2023, Science, 380, 599
Arcus W. R., Macquart J. P., Sammons M. W., James C. W., Ekers R. D., 2021, MNRAS, 501, 5319
Arias M., Timmerman R., Sweijen F., van Weeren R. J., Bassa C. G., 2025, A&A, 699, A319
Astropy Collaboration, 2013, A&A, 558, A33
Astropy Collaboration, 2018, AJ, 156, 123
Astropy Collaboration, 2022, ApJ, 935, 167
Backer D. C., Wong T., Valanju J., 2000, ApJ, 543, 740
Barr E. D. et al., 2013, MNRAS, 435, 2234
Barsdell B. R., 2012, PhD thesis, Swinburne University of Technology, Australia
Bassa C. G. et al., 2017, ApJ, 843, L8
Bhardwaj M. et al., 2025, ApJ, 992, L35
Bhusare Y., Maan Y., Kumar A., 2025, ApJ, 993, 234
CHIME/FRB Collaboration, 2021, ApJS, 257, 59
CHIME/FRB Collaboration, 2023, ApJ, 947, 83
CHIME/FRB Collaboration, 2025, ApJ, 989, L48
CHIME/FRB Collabortion,, 2021, Astron. Telegram, 14497, 1
Chatterjee S. et al., 2017, Nature, 541, 58
Connor L. et al., 2025, Nat. Astron., 9, 1226
Cook A. M. et al., 2023, ApJ, 946, 58
Cooper A. J., Wijers R. A. M. J., 2021, MNRAS, 508, L32
Cordes J. M., Chatterjee S., 2019, ARA&A, 57, 417
Cordes J. M., Lazio T. J. W., 2002, preprint (astro-ph/0207156)
Cordes J. M., Wasserman I., Hessels J. W. T., Lazio T. J. W., Chatterjee S., Wharton R. S., 2017, ApJ, 842, 35
Cordes J. M., Ocker S. K., Chatterjee S., 2022, ApJ, 931, 88
da Costa-Luis C. et al., 2024, tqdm: A fast, Extensible Progress Bar for Python and CLI. https://doi.org/10.5281/zenodo.14231923 (accessed November 24)
Crawford D. F., Jauncey D. L., Murdoch H. S., 1970, ApJ, 162, 405
Daszuta M., Lewandowski W., Kijak J., 2013, MNRAS, 436, 2492
Desvignes G., Barott W. C., Cognard I., Lespagnol P., Theureau G., 2011, in Burgay M., D'Amico N., Esposito P., Pellizzoni A., Possenti A., eds, AIP Conf. Ser. Vol. 1357, Radio Pulsars: An Astrophysical Key to Unlock the Secrets of the Universe. AIP, New York, p. 349
Dey A. et al., 2019, AJ, 157, 168
Eftekhari T. et al., 2025, ApJ, 979, L22
Er X., Yang Y.-P., Rogers A., 2020, ApJ, 889, 158
Ester M., Kriegel H.-P., Sander J., Xu X., 1996, in Pfitzner D. W., Salmon J. K., eds, Second International Conference on Knowledge Discovery and Data Mining (KDD'96). Proceedings of a conference held August 2–4. p. 226 AAAI Press Portland, Oregon
Everett J. E., Weisberg J. M., 2001, ApJ, 553, 341
Faber J. T. et al., 2024, ApJ, 974, 274
Feng Y. et al., 2024, ApJ, 974, 296
Geiger A. et al., 2025, ApJ, 986, 191
Gommers R. et al., 2025, scipy/scipy: SciPy 1.16.0. https://doi.org/10.5281/zenodo.15716342 (accessed January 26)
Gopinath A. et al., 2024, MNRAS, 527, 9872
Guillemot L., Cognard I., van Straten W., Theureau G., Gérard E., 2023, A&A, 678, A79
Harris C. R. et al., 2020, Nature, 585, 357
Hessels J. W. T. et al., 2019, ApJ, 876, L23
Hester J. J., 2008, ARA&A, 46, 127
Hewitt D. M. et al., 2022, MNRAS, 515, 3577
Hewitt D. M. et al., 2023, MNRAS, 526, 2039
Hewitt D. M. et al., 2024a, MNRAS, 529, 1814
Hewitt D. M. et al., 2024b, ApJ, 977, L4
Hotan A. W., van Straten W., Manchester R. N., 2004, PASA, 21, 302
Huang Y.-X. et al., 2025, Res. Astron. Astrophys., 25, 085009
Hunter J. D., 2007, Comput. Sci. Eng., 9, 90
Ioka K., Zhang B., 2020, ApJ, 893, L26
Jahns J. N. et al., 2023, MNRAS, 519, 666
James C. W., Ekers R. D., Macquart J. P., Bannister K. W., Shannon R. M., 2019, MNRAS, 483, 1342
Kader Z., Dobbs M., Leung C., Masui K. W., Sammons M. W., 2024, Phys. Rev. D, 110, 123027
Keimpema A. et al., 2015, Exp. Astron., 39, 259
Kirsten F. et al., 2022, Nature, 602, 585
Kirsten F. et al., 2024, Nat. Astron., 8, 337
Kluyver T. et al., 2016, in Loizides F., Schmidt B., eds, Positioning and Power in Academic Publishing: Players, Agents and Agendas. p. 87 IOS Press
Konijn D. C. et al., 2024, MNRAS, 534, 3331
Krishnakumar M. A., Mitra D., Naidu A., Joshi B. C., Manoharan P. K., 2015, ApJ, 804, 23
Kumar A., Panda U., Bhusare Y., Maan Y., Roy J., Bhattacharyya S., Dudeja C., Lal B., 2024, Astron. Telegram, 16745, 1

Lambert H. C., Rickett B. J., 1999, ApJ, 517, 299
Li D. et al., 2021, Nature, 598, 267
Li Y. et al., 2026, Science 391 280–284
Lyne A. G., Thorne D. J., 1975, MNRAS, 172, 97
Lyne A. G., Pritchard R. S., Graham-Smith F., 2001, MNRAS, 321, 67
Macquart J. P., Ekers R., 2018, MNRAS, 480, 4211
Macquart J. P. et al., 2020, Nature, 581, 391
Main R. et al., 2018, Nature, 557, 522
Marcote B. et al., 2017, ApJ, 834, L8
Marcote B. et al., 2020, Nature, 577, 190
McKee J. W., Lyne A. G., Stappers B. W., Bassa C. G., Jordan C. A., 2018, MNRAS, 479, 4216
McKinney W., 2010, in van der Walt S., Millman J., eds, Proceedings of the 9th Python in Science Conference. p. Austin, Texas 56
McKinven R., CHIME/FRB Collaboration,, 2022, Astron. Telegram, 15679, 1
Mckinven R. et al., 2023a, ApJ, 950, 12
Mckinven R. et al., 2023b, ApJ, 951, 82
Michilli D. et al., 2018, Nature, 553, 182
Moroianu A. M. et al., 2026, ApJ, 996, L16
Ng C. et al., 2025, ApJ, 982, 154
Nimmo K. et al., 2021, Nat. Astron., 5, 594
Nimmo K. et al., 2022, Nat. Astron., 6, 393
Nimmo K. et al., 2023, MNRAS, 520, 2281
Nimmo K. et al., 2025, Nature, 637, 48
Niu C. H. et al., 2022, Nature, 606, 873
Ocker S. K., Cordes J. M., 2024, Res. Notes Am. Astron. Soc., 8, 17
Ocker S. K., Cordes J. M., Chatterjee S., Li D., Niu C.-H., McKee J. W., Law C. J., Anna-Thomas R., 2023, MNRAS, 519, 821
Oostrum L. C. et al., 2020, A&A, 635, A61
Ord S. M., van Straten W., Hotan A. W., Bailes M., 2004, MNRAS, 352, 804
Ould-Boukattine O. S., Hessels J. W. T., Snelders M. P., Kirsten F., Blaauw R., Sluman J. J., Mulder H., 2024, Astron. Telegram, 16732, 1
Ould-Boukattine O. S. et al., 2026, MNRAS, 545, staf1937
Pearlman A. B., Majid W. A., Prince T. A., Kocz J., Horiuchi S., 2018, ApJ, 866, 160
Perez F., Granger B. E., 2007, Comput. Sci. Eng., 9, 21
Petroff E., Keith M. J., Johnston S., van Straten W., Shannon R. M., 2013, MNRAS, 435, 1610
Piro A. L., Gaensler B. M., 2018, ApJ, 861, 150
Planck Collaboration VI, 2020, A&A, 641, A6
Platts E. et al., 2021, MNRAS, 505, 3041
Plavin A., Paragi Z., Marcote B., Keimpema A., Hessels J. W. T., Nimmo K., Vedantham H. K., Spitler L. G., 2022, MNRAS, 511, 6033
Pleunis Z. et al., 2021, ApJ, 923, 1
Rajwade K. M., van den Eijnden J., 2023, A&A, 673, A136
Ransom S., 2011a, Astrophysics Source Code Library, record ascl:1107.017
Ransom S., 2011b, Astrophysics Source Code Library, record ascl:1107.017
Serafin Nadeau T., van Kerkwijk M. H., Bassa C. G., Stappers B. W., Mickaliger M. B., Lyne A. G., 2024, ApJ, 962, 57
Seymour A., Michilli D., Pleunis Z., 2019, Astrophysics Source Code Library, record ascl:1910.004
Shah V. et al., 2025, ApJ, 979, L21
Shin K., CHIME/FRB Collaboration,, 2024, Astron. Telegram, 16420, 1
Simha S. et al., 2023, ApJ, 954, 71
Singha J. et al., 2024, MNRAS, 535, 1184
Snelders M. P., 2022, Master's thesis, University of Amsterdam, https://scripties.uba.uva.nl/search?id = record_30148
Snelders M. P. et al., 2025, preprint (arXiv:2510.11352)
Spitler L. G. et al., 2014, ApJ, 780, L3
van Straten W., 2004, ApJS, 152, 129
van Straten W., 2013, ApJS, 204, 13
van Straten W., Bailes M., 2011, PASA, 28, 1
Temim T. et al., 2024, ApJ, 968, L18
Tendulkar S. P. et al., 2017, ApJ, 834, L7
The pandas development team, 2025, pandas-dev/pandas: Pandas. https://doi.org/10.5281/zenodo.15831829 (accessed January 26)
Tian J. et al., 2024, Astron. Telegram, 16690, 1
Tian J. et al., 2025, MNRAS, 540, 1685
Trimble V., 1971, in Davies R. D., Graham-Smith F., eds, IAU Symposium Vol. 46, The Crab Nebula. p. Springer Dordrecht, The Netherlands 12
Van Rossum G., Drake F. L., 2009, Python 3 Reference Manual. CreateSpace, Scotts Valley, CA
Virtanen P. et al., 2020, Nat/ Methods, 17, 261
Wadiasingh Z., Timokhin A., 2019, ApJ, 879, 4
Wagg T., Broekgaarden F. S., 2024, preprint (arXiv:2406.04405)
Wagg T., Broekgaarden F., Gültekin K., 2024, TomWagg/software-citation-station: v1.2. https://doi.org/10.5281/zenodo.13225824 (accessed November 25)
Wang F. Y., Zhang G. Q., Dai Z. G., Cheng K. S., 2022, Nat. Commun., 13, 4382
Wang P. et al., 2022, The Astronomer's Telegram, 15619, 1
Wang P. et al., 2025, preprint (arXiv:2507.15790)
Whitney A., Kettenis M., Phillips C., Sekido M., 2010, in Navarro R., Rogstad S., Goodhart C. E., Sigman E., Soriano M., Wang D., White L. A., Jacobs C. S., eds, Sixth International VLBI Service for Geodesy and Astronomy. Proceedings from the 2010 General Meeting. p. NASA 192
Xu H. et al., 2022, Nature, 609, 685
Yang Y.-P., Zhang B., 2017, ApJ, 847, 22
Yao J. M., Manchester R. N., Wang N., 2017, ApJ, 835, 29
Zhang B., 2022, ApJ, 925, 53
Zhang B., Hu R.-C., 2025, ApJ, 994, L20
Zhang J. et al., 2025, Astron. Telegram, 17156, 1
Zhang S. B. et al., 2024, Nat. Commun., 15, 7454

SUPPORTING INFORMATION

Supplementary data are available at *MNRAS* online.

Table D1. Burst properties for the burst sample detected using HyperFlash.
Table D2. Properties of the bursts detected using the Nançay Radio Telescope (NRT).

Please note: Oxford University Press is not responsible for the content or functionality of any supporting materials supplied by the authors. Any queries (other than missing material) should be directed to the corresponding author for the article.

APPENDIX A: OBSERVATIONAL CAMPAIGN

An overview of the observational campaign is given in Fig. B1. Additionally, the logs of the observations is provided in `.csv` format in the Supplementary Material.

APPENDIX B: DYNAMIC SPECTRA OF WESTERBORK BURSTS

The time series and dynamic spectra of a subsect of bursts detected by Westerbork are shown in Fig. B2.

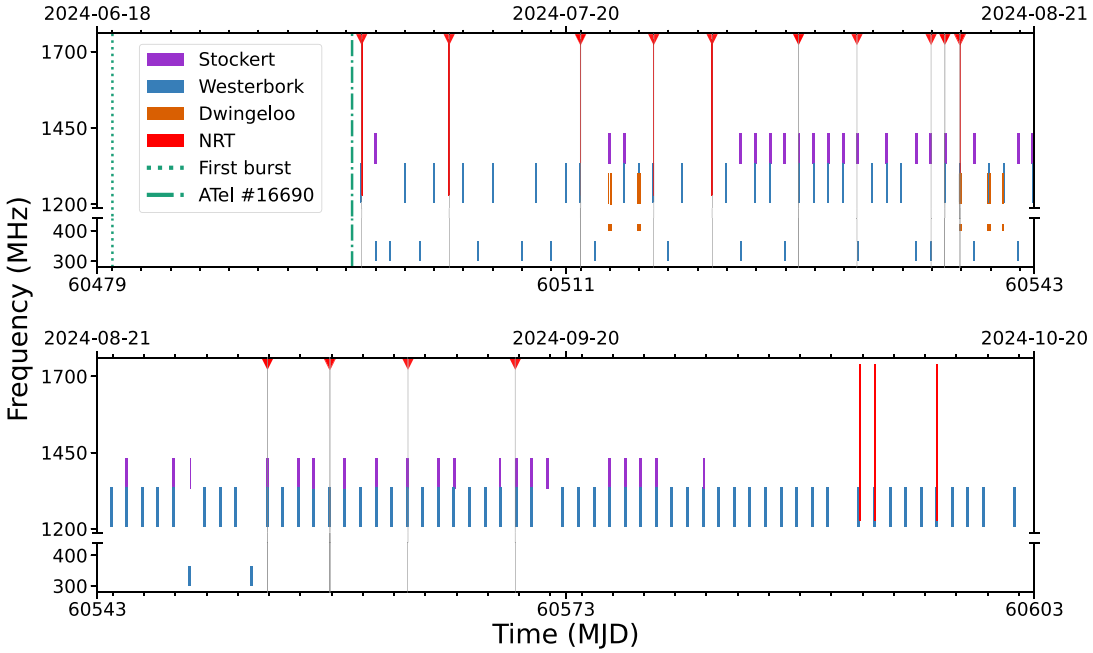

Figure B1. Overview of the observing campaign targeting FRB 20240619D. Each coloured block represents an observation conducted with a specific telescope at a given frequency, where the block height is proportional to the observing bandwidth and the block width reflects the observation duration. The *x*-axis shows time in both MJD and calendar date; the top panel spans 64 d and the bottom panel 60 days. The broken *y*-axis indicates the frequency range of the observations. Red triangles, together with black vertical lines, mark the observations during which bursts were detected. In the top left of the plot, a dotted green line indicates the time of the first burst detected with MeerKAT, and a dash-dotted line marks the publication of the discovery ATel. Our observing campaign began 13 hours after the ATel was published.

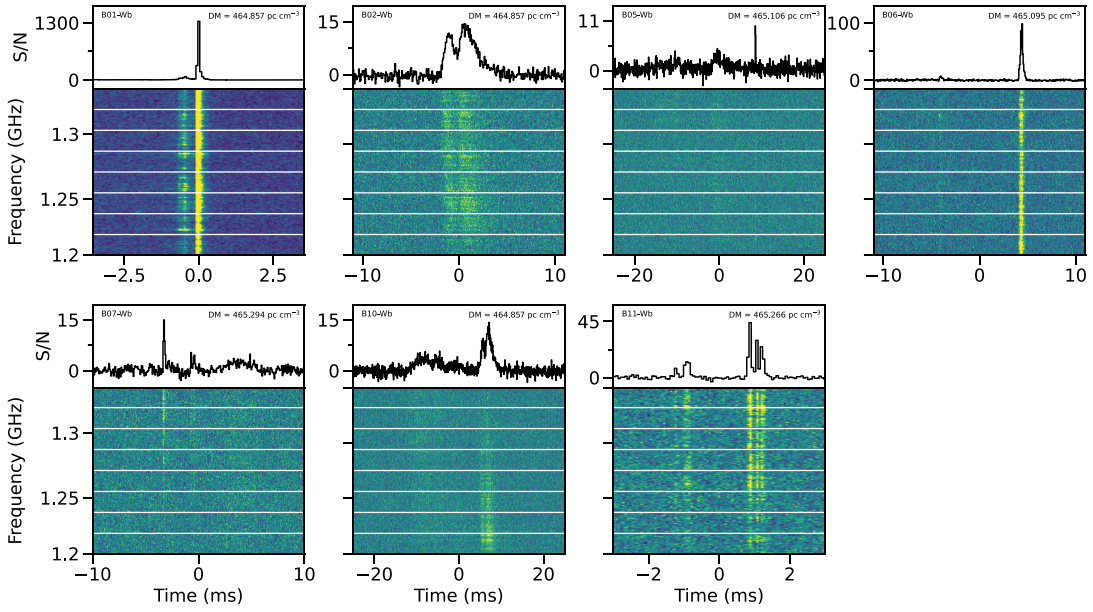

Figure B2. Time series (top panels) and dynamic spectra (bottom panels) for a subset of bursts that were detected by Westerbork, and for which voltage data was saved. The time and frequency resolution of all bursts shown here is 64 µs and 500 kHz, respectively. The bursts have been coherently dedispersed using `SFXC` to the indicated DM in the top right. The white lines are zapped channels at the edges of the eight subbands used in the recording of the data. This plot illustrates that FRB 20240619D bursts show complex temporal structures ranging from microseconds (B01–Wb) to milliseconds (B02–Wb).

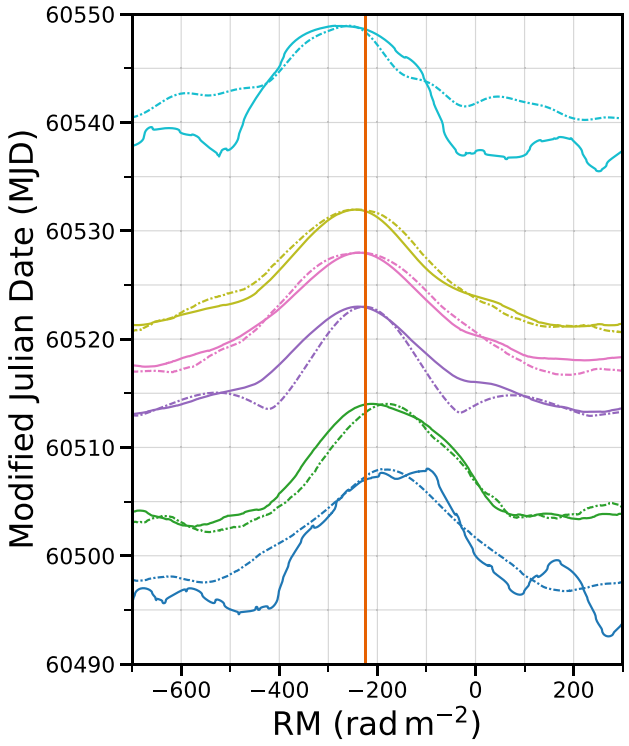

Figure C1. FDFs for the multiple ÉCLAT-detected bursts. The solid and dashes lines show the FDFs obtained from two different bursts selected from each observation and calibrated with the PCM file from MJD 60598. The vertical distance between FDFs corresponds to their time separation. More noisy FDFs correspond to weaker bursts.

APPENDIX C: POLARIZATION CALIBRATION

We calibrated the polarimetry of our NRT data with the full receptor model (S. M. Ord et al. 2004; W. Straten 2004), using both the noise diode scan from each observation and a polarization calibration modelling (PCM) file. By rotating the receiver horn by 180° over the course of a 1-h observation of the pulsar PSR J0742−2822, wide parallactic angle variations can be imitated, which in turn can be used to fully take into account the non-orthogonality of the receptor hands. This method has previously been used for polarisation calibration of pulsar data from the NRT (L. Guillemot et al. 2023). Unfortunately, due to maintenance at the NRT, PCM files were only obtained on MJD 60499 and thereafter MJD 60598. We calibrated the data using both PCM files, ran rmfit to obtain a FDF, and fit a Gaussian to the central peak, shown in Fig. C1. Typically the RM values differ by $\lesssim 6$ per cent between the two PCM files, and we thus conclude that the change in the absolute RM we see over the activity period (right panel in Fig. 1) is not the result of inaccurate calibration.

APPENDIX D: BURST PROPERTY TABLES

Burst properties from the HyperFlash and ÉCLAT observing campaigns are presented in Tables D1 and D2. The full tables are provided in `.csv` format as part of the Supplementary Material and are also available on GitHub and Zenodo.

Table D1. Burst properties for the burst sample detected using HyperFlash. The full table is also available in `.csv` format in the Supplementary Material.

Burst ID	Station	TOA[a] [MJD]	Peak S/N	Fluence[b] [Jy ms]	Width [ms]	BW[c] [MHz]	DM [pc cm^3]
B01	wb	60511.994427	750.47	771.73 ± 154.35	27.71	128	464.857 ± 0.003
B02	st	60526.896118	17.98	100.75 ± 20.15	6.99	98	–
B02	wb	60526.896127	15.96	154.56 ± 30.91	8.58	128	–
B03	st	60530.882722	11.85	70.26 ± 14.05	24.47	98	–
B04	st	60535.945584	31.62	171.98 ± 34.40	27.96	98	–
B05	st	60536.884172	6.06	30.58 ± 6.12	10.49	98	–
B05	wb	60536.884182	10.10	102.92 ± 20.58	25.47	128	465.106 ± 0.013
B06[†]	dw	60537.888446	–	–	∼1.00	200	–
B06	wb	60537.888455	86.19	104.17 ± 20.83	9.79	128	465.095 ± 0.010
B07	st	60553.898090	10.67	27.11 ± 5.42	6.12	98	–
B07	wb	60553.898099	16.28	41.32 ± 8.26	10.30	128	465.294 ± 0.079
B08	wb	60557.865193	13.78	108.16 ± 21.63	10.75	128	–
B09	wb	60557.912320	9.85	8.10 ± 1.62	3.84	128	–
B10	wb	60562.892980	13.90	224.60 ± 44.92	22.98	128	–
B11	wb	60569.762476	35.32	47.13 ± 9.43	3.52	128	465.266 ± 0.016

Notes.[†]B06-dw is included, but fluence measurements were unavailable due to RFI; width and bandwidth were manually estimated.
[a]Time of arrival referenced to the solar system barycentre at infinite frequency in TDB. We adopt the DM of 464.857 pc cm^{-3} for all bursts except for those for which we optimized the DM (Section 3.1.1). We assume a dispersion constant of $\mathcal{D} = 1/(2.41 \times 10^{-4})$ MHz^2 pc^{-1} cm^3 s. The position of Stockert is $X = 4031510.647$ m, $Y = 475159.114$ m and $Z = 4903597.840$ m. The position of Westerbork is $X = 3828750.6969$ m, $Y = 442589.2176$ m and $Z = 5064921.5700$ m; see the EVN station locations page.
[b]We assume a 20% error for all bursts dominated by the uncertainty on the SEFD. For Westerbork the SEFD is retrieved from the EVN status page
[c]Measured bandwidth used to compute fluence.

Table D2. Properties of the bursts detected using the Nançay Radio Telescope (NRT). The full table is available in `.csv` format in the Supplementary Material.

Burst index (NRT)	TOA[a] (MJD)	Peak flux (Jy)	Fluence[b] (Jy ms)	Width[c] (ms)	Bandwidth[c] (MHz)	RM[d] (rad m^{-2})	RM[d] (rad m^{-2})
B01	60497.026715	0.62	0.76 ± 0.15	0.76	144	–	–
B02	60497.026983	1.63	3.89 ± 0.78	3.88	188	-182.2 ± 31.9	-187.4 ± 28.2
B03	60497.027644	0.82	2.36 ± 0.47	2.36	432	–	–
B04	60497.031234	0.62	0.98 ± 0.12	0.98	428	–	–
B05	60497.033447	0.73	1.24 ± 0.25	1.24	188	–	–
⋮	⋮	⋮	⋮	⋮	⋮	⋮	⋮
B202	60537.918644	0.80	3.37 ± 0.67	3.37	184	–	–
B203	60537.922310	1.20	0.76 ± 0.15	0.76	184	–	–
B204	60537.932108	0.72	1.40 ± 0.28	1.40	112	–	–
B205	60537.935503	3.05	1.81 ± 0.36	1.80	232	-254.9 ± 43.1	-272.4 ± 30.6
B206	60537.937718	0.72	1.01 ± 0.20	1.00	184	-279.8 ± 46.9	-270.3 ± 30.2

[a]Time of arrival referenced to the solar system barycentre at infinite frequency in TDB. We adopt a DM of 464.86 pc cm^{-3} for all bursts in the NRT sample, assuming a dispersion constant of $\mathcal{D} = 1/(2.41 \times 10^{-4})$ MHz^2 pc^{-1} cm^3 s, reference frequency of 1738 MHz and source position as published in the discovery ATel of: $\alpha = 19^{\rm h}49^{\rm m}29.21^{\rm s}$, $\delta = -25^\circ 12' 49.40''$ (J2000) (J. Tian et al. 2024). The position of NRT is: $X = 4324165.81$ m, $Y = 165927.11$ m and $Z = 4670132.83$ m.
[b]We assume a 20% error for all bursts, dominated by the uncertainty on the SEFD.
[c]Manually determined bandwidth and width used to compute fluence.
[d]Calibrated using the polarization calibration model (PCM) of MJD 60499 and 60598; see Appendix C.

APPENDIX E: PROBING THE NARROWEST FREQUENCY SCALE

In Fig. E1, we show a measurement and tentative detection of the ∼6 kHz scale for B01-Wb.

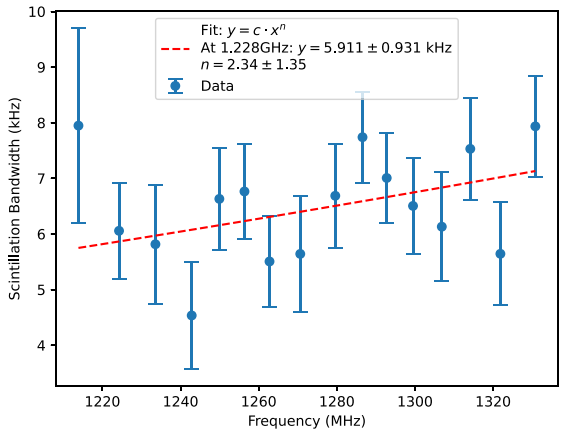

Figure E1. A measurement of the ∼6 kHz scale across 16 subbands in the burst spectrum of B01–Wb. The frequency scale is measured across all subbands with a power-law frequency dependence of $\nu^{\alpha=2.34\pm1.35}$.

APPENDIX F: DM OPTIMISATION FOR BURST B26-NRT

In Fig. F1 we show the DM optimisation of the bright burst detected, B26-NRT.

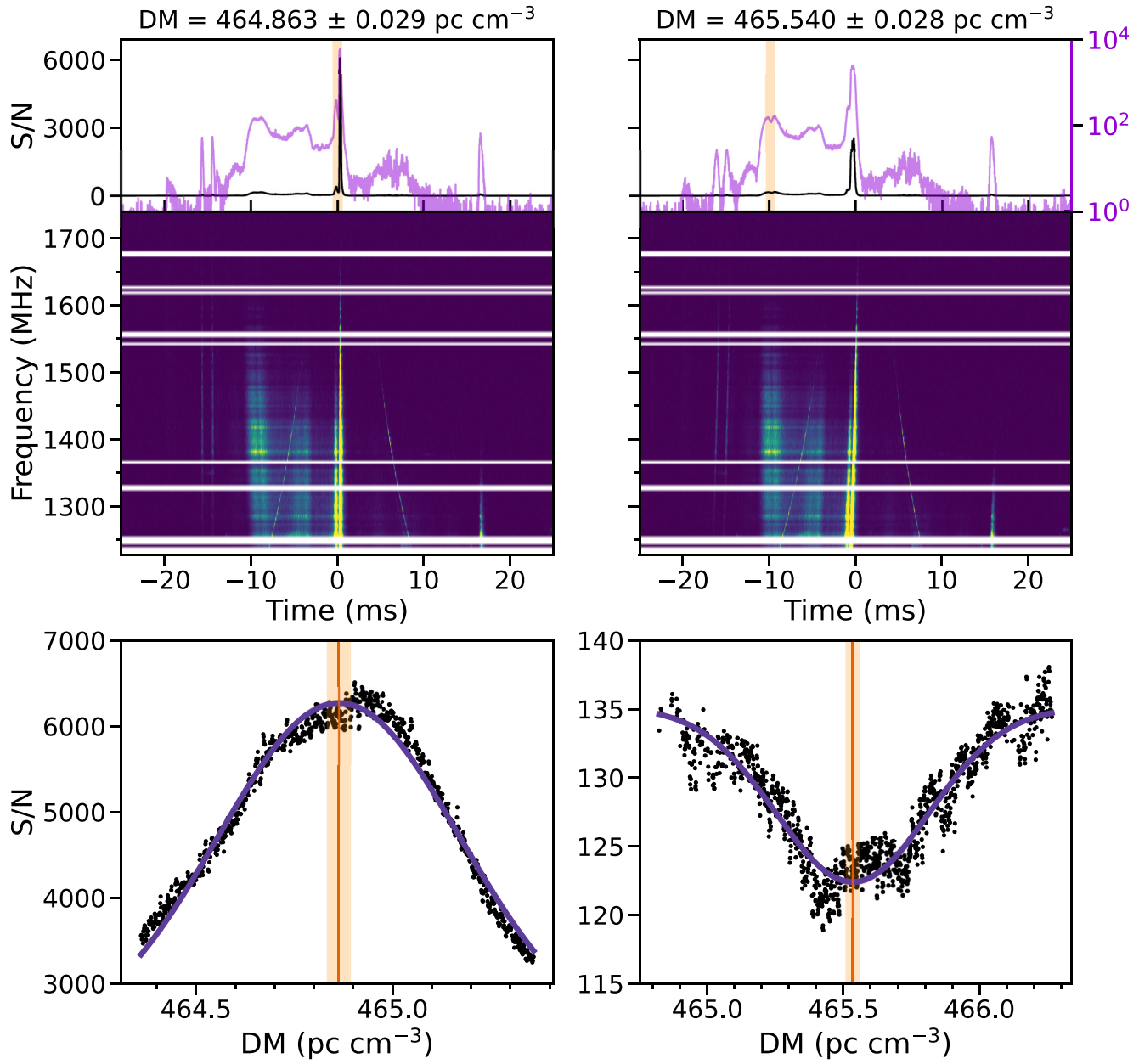

Figure F1. The brightest burst (B26–NRT) in the sample detected by NRT, dedispersed to two different DM values. The top panels display the dynamic spectrum and time series of the burst, with a yellow-highlighted region indicating the time window used to measure the peak S/N. We show the time series on both linear (black line) and logarithmic scales (purple line). The bottom panel shows the Gaussian fit: the solid orange line marks the best-fit value, and the yellow shaded region indicates the uncertainty on the DM.

This paper has been typeset from a TEX/LATEX file prepared by the author.